
HIM 1990-2015

2013

Microscopic Surface Textures Created by Interfacial Flow Instabilities

Jing Gu
University of Central Florida

 Part of the [Mechanical Engineering Commons](#)

Find similar works at: <https://stars.library.ucf.edu/honorstheses1990-2015>

University of Central Florida Libraries <http://library.ucf.edu>

This Open Access is brought to you for free and open access by STARS. It has been accepted for inclusion in HIM 1990-2015 by an authorized administrator of STARS. For more information, please contact STARS@ucf.edu.

Recommended Citation

Gu, Jing, "Microscopic Surface Textures Created by Interfacial Flow Instabilities" (2013). *HIM 1990-2015*. 1497.

<https://stars.library.ucf.edu/honorstheses1990-2015/1497>

MICROSCOPIC SURFACE TEXTURES CREATED BY INTERFACIAL
FLOW INSTABILITIES

by

JING GU

A thesis submitted in partial fulfillment of the requirements
for the Honors in the Major Program in Mechanical Engineering
in the College of Engineering and Computer Science
and in The Burnett Honors College
at the University of Central Florida
Orlando, Florida

Summer Term, 2013

Thesis Chair: Weiwei Deng, Ph.D.

© 2013 Jing Gu

ABSTRACT

In nature, microscopic surface textures impact useful function, such as the drag reduction of shark skin (Dean & Bhushan, 2010) and superhydrophobicity of the lotus leaf (Pan, Kota, Mabry, & Tuteja, 2013). In this study, we explore these phenomena by re-creating microscopic surface textures via the method of interfacial flow instability in drying polyvinylidene fluoride (PVDF) acetone solutions. In general, PVDF films can be made using either spin coating or electrospray deposition with various weight concentrations in acetone.

In order to study the morphology of the porous structure of PVDF films, wet deposition samples were fabricated by spin coating or near-field electrospray. Possible theories are discussed and examined to explain the formation of these porous structures resulting in development of a well-controlled method to create porous PVDF films with various pore sizes and pore densities. All samples are characterized and found to exhibit superhydrophobicity and drag reduction. To connect porous PVDF film morphology to the established field of dry particle fabrication, PVDF particle synthesis by far-field electrospray is also reviewed and discussed. An established method to generate polymer particles of different morphologies in other polymers (Almería-Díez, 2012) by electrospray drying is confirmed using PVDF as well.

Due to the ability of scalable and re-configurable electrospray, the microscopic surface textures can be applied to areas of any size to reduce drag or impart water-repelling properties.

DEDICATION

This thesis is dedicated to the loving memory of Aimée Lu.

ACKNOWLEDGEMENTS

A huge thank you to my thesis adviser, Dr. Weiwei Deng. Without his guidance and support, this work would not have been possible. I deeply appreciate your patience and diligence in guiding me towards becoming a professional researcher and engineer. I am standing on the shoulders of giants.

I express my deepest gratitude to all my lab mates, special thanks to Dr. Cheng Li and Yan Wei for their guidance and patience. Without them, this work would not have been possible. Thank you to my family and friends for supporting me through the years during my thesis work. Because of you all, I have been inspired to embark on this journey and have been motivated to push it through to its completion.

TABLE OF CONTENTS

CHAPTER 1: INTRODUCTION.....	1
1.1 Surface Texture And Its Applications.....	1
1.1.1 <i>Surface texture modifies the interaction of surface and surrounding environment</i>	1
1.1.2 <i>Microscopic surface textures can be multifunctional</i>	3
1.2 The Challenge Of Fabricating Microscopic Surface Texture With Large Area.....	7
CHAPTER 2: RESEARCH METHODS	9
2.1 Materials.....	9
2.1.1 <i>Key materials: PVDF/Kynar</i>	9
2.1.2 <i>Solvents</i>	10
2.2 Film Fabrication.....	12
2.2.1 <i>Spin coating</i>	12
2.2.2 <i>Electrospray</i>	14
2.3 Spray Characterization	24
CHAPTER 3: RESULTS AND DISCUSSION.....	27
3.1 Dry Deposition.....	27
3.1.1 <i>Rayleigh instability and Coulombic fission</i>	27
3.1.2 <i>Spray drying mechanism</i>	28
3.1.3 <i>The effect of film morphology to contact angle</i>	32
3.2 Wet Deposition	35
3.2.1 <i>Honeycomb morphology</i>	35

3.2.2 The effect of solvent volatility.....	40
3.2.3 <i>Control of the average pore size</i>	44
3.2.4 <i>Drag reduction of honeycomb texture</i>	47
CHAPTER 4: CONCLUSIONS	50
BIBLIOGRAPHY	52

LIST OF FIGURES

Figure 1: (a) Golf Ball (b) Nike Tracksuit (c) Dimpled Car	2
Figure 2: Flow Past a Smooth Ball and a Dimpled Ball	3
Figure 3: Drag Coefficient vs. Rayleigh Number	3
Figure 4: Shark Skin.....	5
Figure 5: Applications Of Microscopic Surface Texture.....	6
Figure 6: Application Areas of Large- area textured Surface (adopted from Kornel F. Ehmann, 2010).....	7
Figure 7 Aluminum, Brass, And Polycarbonate Nozzles	8
Figure 8: MTI Corporation VTC-100A Spin Coater.....	13
Figure 9: Viscosity vs. Concentration	13
Figure 10: Typical Electrospray.....	15
Figure 11: (a) The ES as a printing head, with near-field and far-field schematically illustrated. (b) ES printing setup	19
Figure 12: Typical PDI setup and system components	24
Figure 13: Top - Schematic of PDI Principle, Bottom - Early generation 15 nozzle device in the PDI, notice the subtle crossing of the two beams in the spray cloud.....	25
Figure 14: Droplet Size vs. Flow Rate	26
Figure 15: Flash-shadowgraphs of electrospray droplets undergoing Coulomb fissions in flight (adopted from (Gomez and Tang 1994)	28
Figure 16: Diverse morphologies obtained in PLGA particles as a result of Coulomb fissions in the precursor droplets. (adopted from Almería-Díez, 2012)	29

Figure 17: Particle Morphology (a)	30
Figure 18: Particle Morphology (b)	30
Figure 19: Overview of PVDF particles synthesized with Acetone, for different solution concentration and solution flow rates.	31
Figure 20: Different States of Superhydrophobicity	33
Figure 21: SEM micrograph of PVDF film	35
Figure 22: Breath Figure Method (adopted from A-G: Srinivasarao et. al, 2001 ; H: Ke, Wan, et. al, 2010; I: Ponnusamy et. al, 2012)	36
Figure 23: Natural Rayleigh–Bénard Convection	38
Figure 24: A solvent-rich fluctuation rises and lowers the surface tension at point A. Thus the fluid is driven from A to B and the fluctuation is amplified. (adopted from Gennes, 2001)	40
Figure 25: PVDF Films Synthesis with NMP and Acetone	43
Figure 26: SEM Micrographs of Samples with Thickness of 22.07, 10.82, 7.26 and 5.46 μm	45
Figure 27: Pore Size vs. Thickness	45
Figure 28: Pore Density vs. Thickness	46
Figure 29: Experimental Setup for Drag Measurement	47
Figure 30: Drag vs. Velocity	48
Figure 31: Drag Coefficient vs. Rayleigh Number	49

LIST OF TABLES

Table 1: Physical Properties of Acetone and NMP.....	11
Table 2: Spin Coating Conditions.....	14
Table 3: Dry Deposition Conditions.....	21
Table 4 : Wet Deposition Conditions with Different Parameters.....	22
Table 5: Wet Deposition Conditions with Different Substrate-Moving Speed.....	23
Table 6: Deposition and Particle Phenomenology with different Flow Rate	34

CHAPTER 1: INTRODUCTION

1.1 Surface Texture And Its Applications

1.1.1 Surface texture modifies the interaction of surface and surrounding environment

"There has been no biological change in humans in 40,000 or 50,000 years. Everything we call culture and civilization we've built with the same body and brain."

—Stephen Jay Gould

When we look back into history, we notice that there is a huge evolution in human beings throughout time. However, we do not see that kind of changes in modern history. But in fact, we are still evolving, subject to the forces of Darwinian natural selection. Our civilization and technology accelerate our “evolution” and make us become smarter, prettier, and *faster*. Because intelligence and beauty are somewhat subjective, a speed improvement will be analyzed. For example, the Men’s 100m sprint world records can be examined. In 1968, Jim Hines set the world records of Men’s 100m Sprint in less than 10 seconds. Fifteen years later, Calvin Smith smashed this world record by only 0.02 second. In the late 20th and the early of 21st centuries, it usually takes two to three years to break the world record by 0.01 or 0.02 second. Given all that, the human being might be said to be evolving. However, with the development of new technology, our evolutionary path may become interrupted. Technology and not necessarily evolution, allows the human animal to run faster.

Nike adopted the concept of golf ball's dimples (Figure 1a) into their design. The dimples on golf ball are proven to reduce drag of a spherical object in flow. (Davies, 1949) Since drag depends on the flow in the boundary layer, we can assume some

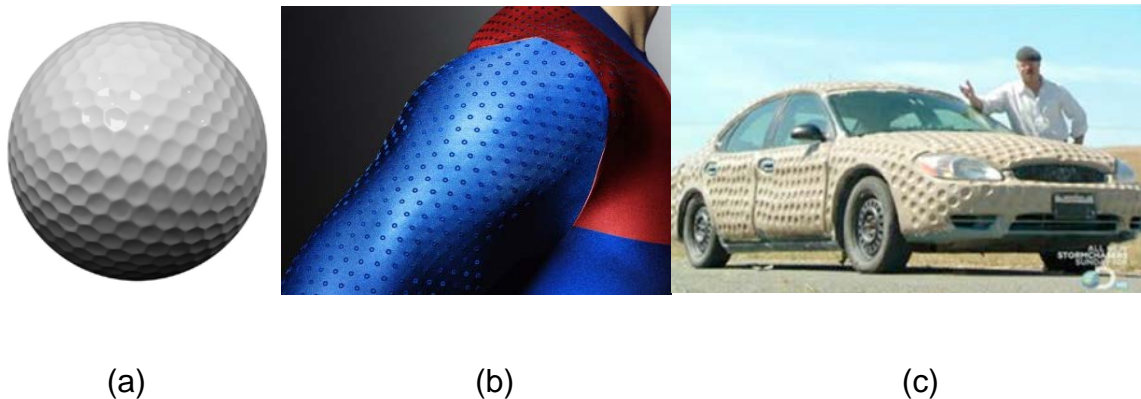


Figure 1: (a) Golf Ball (b) Nike Tracksuit (c) Dimpled Car

changes with surface roughness. Figure 2 shows the observation of a smooth ball and a dimpled ball. The dimples on the ball turbulate the boundary layer and reduce the drag by suppressing the flow separation. Figure 3 shows the relationship between drag coefficient and Reynolds number for a smooth ball and a golf ball. The drag coefficient of the golf ball at different Rayleigh number is shown in red dashed line and the smooth ball is shown in blue line. The result indicates that there is a range of Reynolds numbers for which the drag of the golf ball is much less than the drag of the smooth ball for the same surface area, velocity and flow conditions. At a higher Reynolds number, the drag coefficient of the golf ball is much less than a smooth ball. Nick utilized this concept and introduced their next generation tracksuit with zoned aerodynamics. It is proved that this kind of surface texture can offers the greatest aerodynamic drag reduction of any Nike uniform to date. Anyone can run 0.023 second faster wearing a Nike tracksuit (Figure

1b). Also, the dimpled car is tested and found out to be 11% better mileage than a smooth finished car.

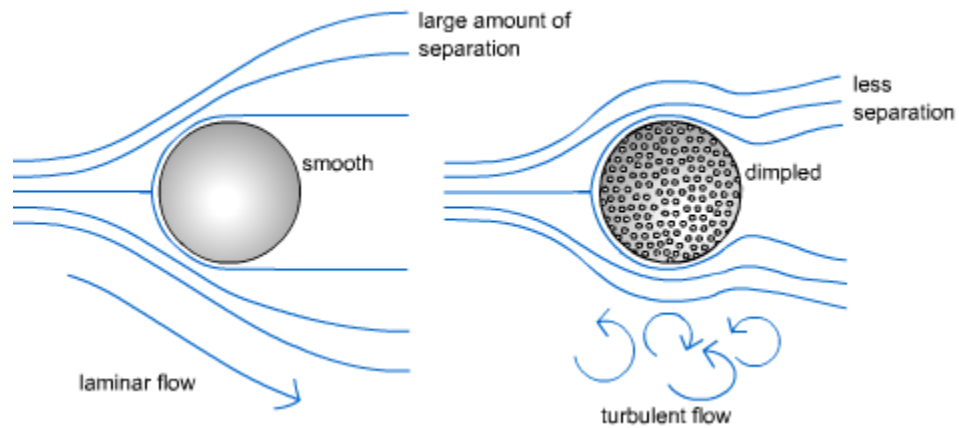


Figure 2: Flow Past a Smooth Ball and a Dimpled Ball

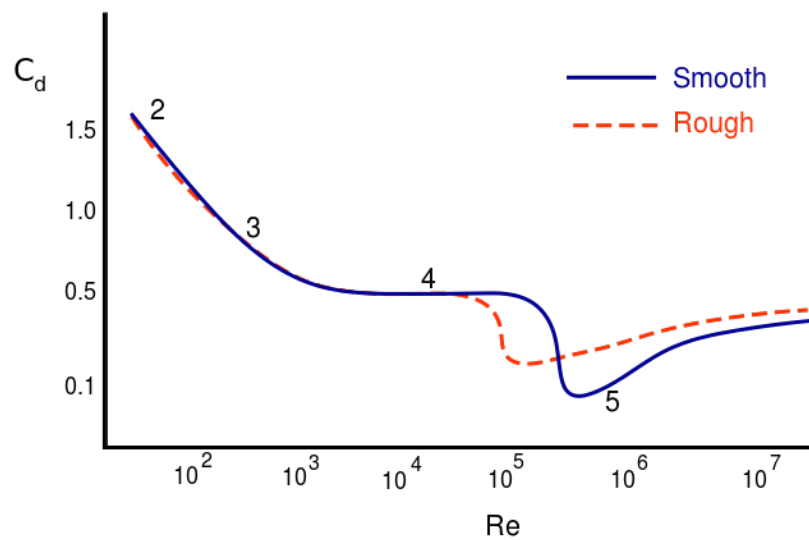


Figure 3: Drag Coefficient vs. Rayleigh Number

1.1.2 Microscopic surface textures can be multifunctional

In the 1200's, one of the most common yet influential instruments in the field of science, microscope, was invented by Roger Bacon. When the most ordinary things in life viewed at a microscopic level, they might be transformed into terrifying masterpiece of art. Not alone Microscopy brought the revolution of science, especially, biology, but made us understand objects in a deeper perspective as well. Because of the evolution of amazing nature and microscopes, more and more different microscopic surface textures have been finding in a different variety of animals. The functions of these different microscopic surface textures include mechanical support, providing protection and motility to organisms but not limit to these (Su, Sanchez, & Yang, 2012). They can also concentrate light, generate color or help sense the environment (Su et al., 2012). They make giant sharks swim faster and protect defenseless butterflies from their hungry predators.

Under optical microscope, the skin of shark exhibits riblet structures (Figure 4). These riblet structures were proven to reduce skin friction drag in the turbulent-flow regime because they always aligned in the direction of flow. Dean et al fabricated the riblets structures of the shark skin for the purpose of study and application that reproduce and improve upon them, and verifying a maximum drag reduction of nearly 10%. (Dean & Bhushan, 2010)

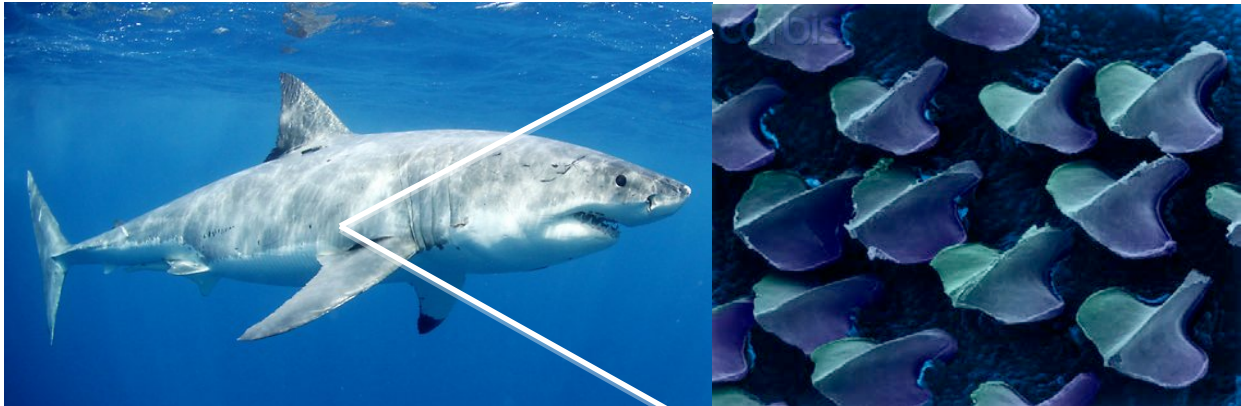
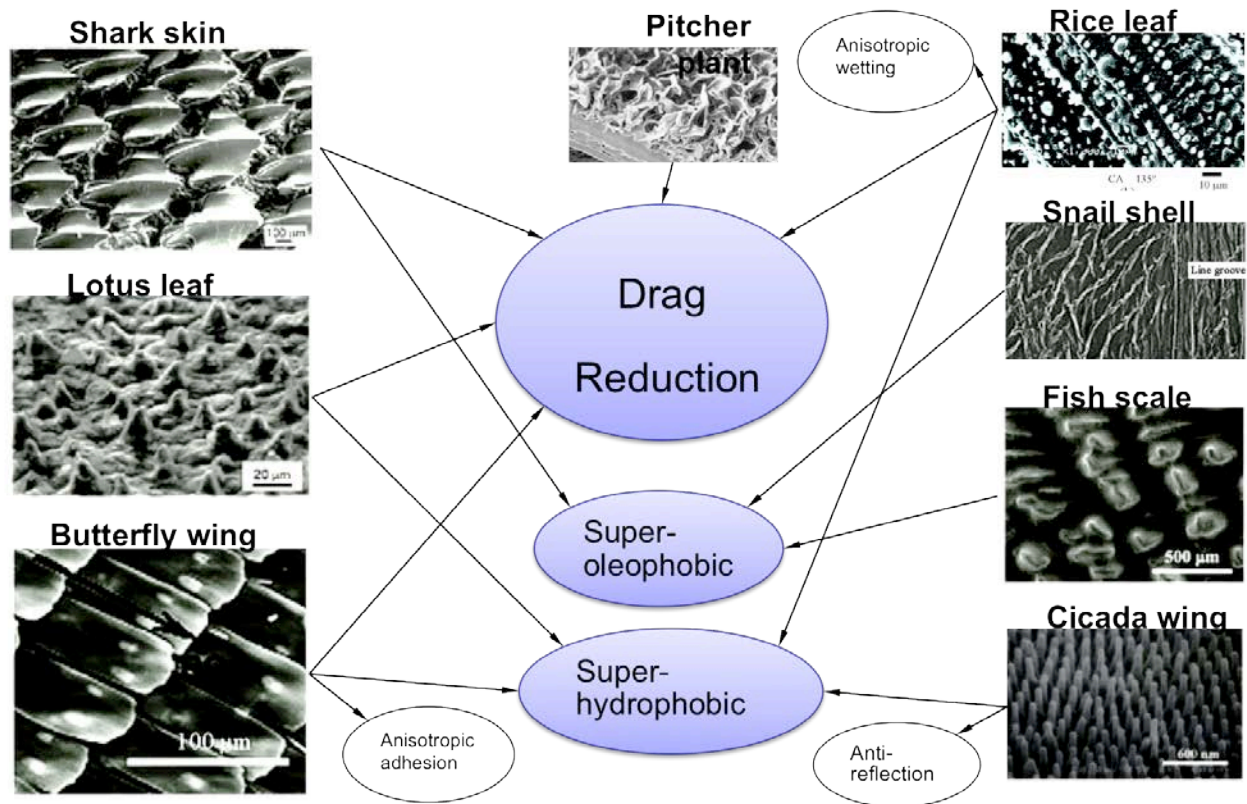


Figure 4: Shark Skin

Nature has been amazing us with her miraculous creatures for many years. Her designs are always beautiful yet efficient, for example, many structures serve multiple purposes. Other than the drag reduction, shark skin also has superoleophobic function, lotus leaves is another good example; their surface possess a hierarchical surface structure that causes drag reduction and superhydrophobic behavior (Pan et al., 2013). Butterfly wing, cicada wing and rice leaf are found with drag reduction and either superhydrophobicity or superoleophobicity (Su et al., 2012). (Figure 5)



6

Figure 5: Applications Of Microscopic Surface Texture

Due to high demand of developing new methodologies in the fabrication of bimodal porous structures, an increasing number of scientists and researchers have been researching in the area of the synthesis and applications of hierarchically structured porous materials in the past decade. Porous materials are materials that contain a porous structure consisting of interconnected pores on within length range from 2nm to 5 μm (Su et al., 2012).

1.2 The Challenge Of Fabricating Microscopic Surface Texture With Large Area

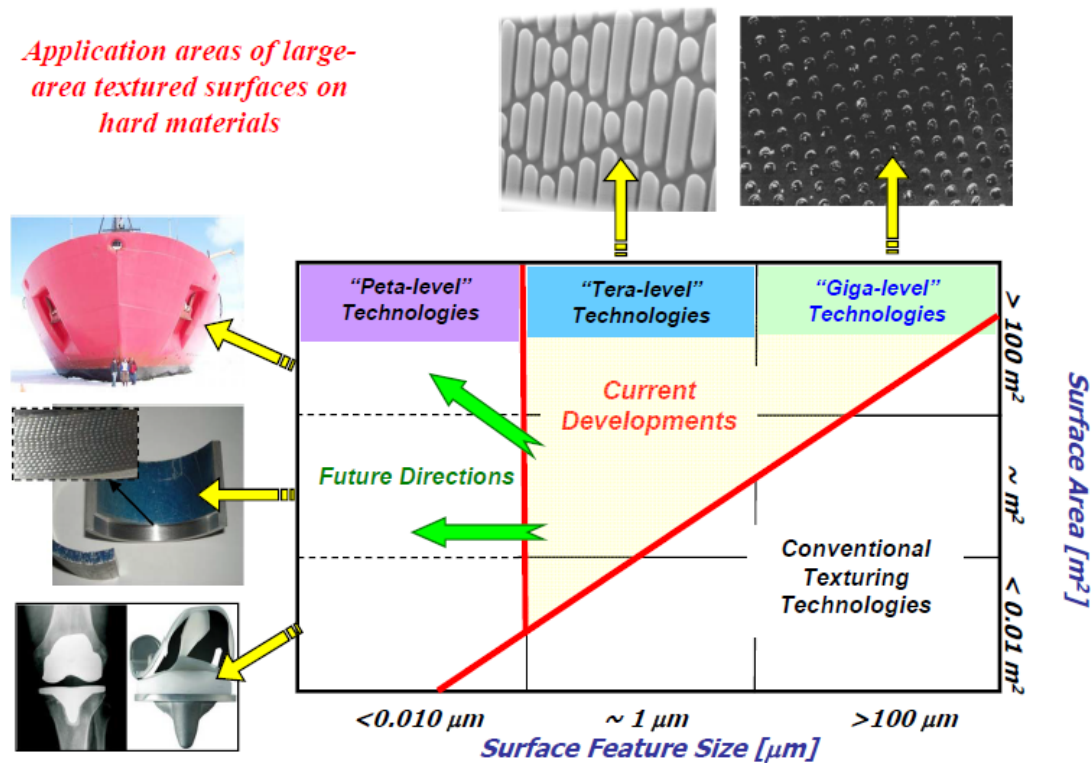


Figure 6: Application Areas of Large- area textured Surface (adopted from Kornel F. Ehmann, 2010)

It is always a challenge to fabricate microscopic surface texture with large area. However, we have shown that the electro spray is scalable and re-configurable. Previously we have demonstrated a silicon micro-fabricated array of up to 331 sources with a packing density of $250 \text{ sources}/\text{cm}^2$ (Deng, Klemic, Li, Reed, & Gomez, 2006). In addition, we demonstrated the concept of digital electro spray (Deng, Waits, & Gomez, 2010) with a 61-source multiplexed electro spray system, in which each individual electro spray source is addressable and can be turned on and off rapidly and

independently. This system exhibited a 100 Hz response frequency. Because nozzles fabricated in silicon could be too fragile for certain applications, we recently expanded the nozzle materials beyond silicon. We successfully applied the precision CNC micro-machining approach in fabricating micro nozzles (120 μm outer diameter and 50 μm inner diameter) on a wide range of materials including aluminum, brass, and polycarbonate (Figure 7).

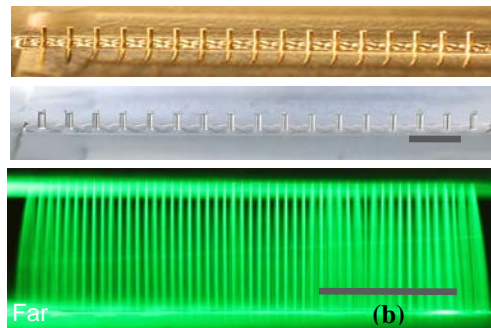


Figure 7 Aluminum, Brass, And Polycarbonate Nozzles

The nozzles to be used in this project will be larger than the one we demonstrated (Figure 7), therefore we will be able to use the same CNC micromachining to fabricate the nozzles we need.

Due to the ability of scalable and re-configurable electrospray, the microscopic surface textures can be applied to areas of any size to reduce drag or impart water-repelling properties.

CHAPTER 2: RESEARCH METHODS

2.1 Materials

2.1.1 Key materials: PVDF/Kynar

Polyvinylidene fluoride (PVDF), also known as KYNAR is a unique engineering material, which has been using for various applications. It can be exposure to harsh thermal, chemical and ultraviolet environments due to its characteristic stability of fluoropolymers. Furthermore, it is soluble in various polar solvents, for example, acetone for coating applications. Because of its chemical and high temperature resistance, it is also used as a contact surface for the production, storage and transfer of corrosive fluids. PVDF resin is used in mechanical components, fabricated vessels, tanks, pumps, valves, filters, heat exchangers, tower packing, piping systems due to its fire-resistance, abrasion resistance, low-smoke emission, chemical and mechanical properties. It is also suitable for protective sheathing, plenum and communications wiring insulation and binder resin for battery manufacture. (THERMOPLASTICS FOR ENGINEERING APPLICATIONS, n.d.)

Due to PVDF's strength, durability and versatility, it is preferred to be used in general coatings and plastic optical fibers. Moreover, the excellent outdoor aging and weathering properties of PVDF led to its use in long-lasting paints for coating metal sheet for the past 40 years. PVDF can also be used to protect thermoplastics through co-extrusion or film lamination techniques to obtain anti-grime and anti-graffiti surfaces

with excellent weathering properties. KYNAR FLEX® 2800-01 is the material we used in the following experiments. It is a functional powder coating material, which enables a thick spray coating of PVDF resin to be applied to metals. (THERMOPLASTICS FOR ENGINEERING APPLICATIONS, n.d.)

2.1.2 solvents

Solvent also plays an important a role in film fabrication. The physical properties of the solvent can affect the possibility of the electrospray and the resulting particle size, particle shape, porous size, porous shape and morphology.

Table 1 lists the two solvents used in spin coating for PVDF and their most relevant physical properties. Parameters such as surface tension, viscosity, evaporation rate and boiling temperature have huge impacts on the final outcome structure and must be carefully considered. All the values have been measured at 20°C unless specified.

In order to select the practical solvent for PVDF coating, we evaluated solvent evaporation rate and polymer diffusion in the solvent. These two major parameters will determine the morphology (porous structure versus smooth surface).

Table 1: Physical Properties of Acetone and NMP

Name	Acetone	NMP
Formula	C ₃ H ₆ O	C ₅ H ₉ NO
Density	791kg/m ³	1028kg/m ³
Molar Mass	58.08g/mol	99.13g/mol
Vapor Pressure (at 25 °C)	30.6Kpa	0.04Kpa
Surface Tension	25.20mN/m	40mN/m
Viscosity	0.331mPa·s	1.7mPa·s
Evaporation Rate	7.7	0.06
Boiling Point	56°C	204.3°C
Melting Point	-95°C	-24°C

2.2 Film Fabrication

Substrate

Prior to spin coating and electrospraying, the silicon wafers were cleaved into 3.5cm × 1.5cm pieces. They were used as substrates in the following experiments after thoroughly cleaned using a sequential rinse in acetone, ethanol, deionized water, and nitrogen gas.

Solution

3% wt. PVDF in acetone, 4% wt. PVDF in acetone, and 5% wt. PVDF in acetone were used in spin coating. In order to generate a stable electrospray, 2% wt. PVDF in acetone, 3% wt. PVDF in acetone, and 4% wt. PVDF in acetone solutions were used in electrospraying. These solutions were required to ultrasonicate for at least 8 minutes prior to loading in the syringe for both spin coating and electrospraying.

2.2.1 Spin coating

MTI Corporation VTC-100A Spin Coater (Figure 8) was used in this part of the experiment. It provides dual speed controls with continuous speed adjustment and individual timer. 'FCN', 'Curs', '+' and '-' bottoms were used to set the spin cycle time and speed for phase I and phase II with the indicating light under 'T1', 'SPD1', 'T2', 'SPD2'. The time and speed for both phase were chose concernedly based on the viscosity of the different concentration. The fundamental of creating a smooth coating is to balance centrifugal forces, which were controlled by spin speed and viscous forces,

which were determined by solution viscosity. Figure 9 shows the viscosity of the solutions versus the concentration of the solution. Also, a summary of the spin coating conditions for the three experiments are presented in Table 2.



(a) (b)
Figure 8: MTI Corporation VTC-100A Spin Coater

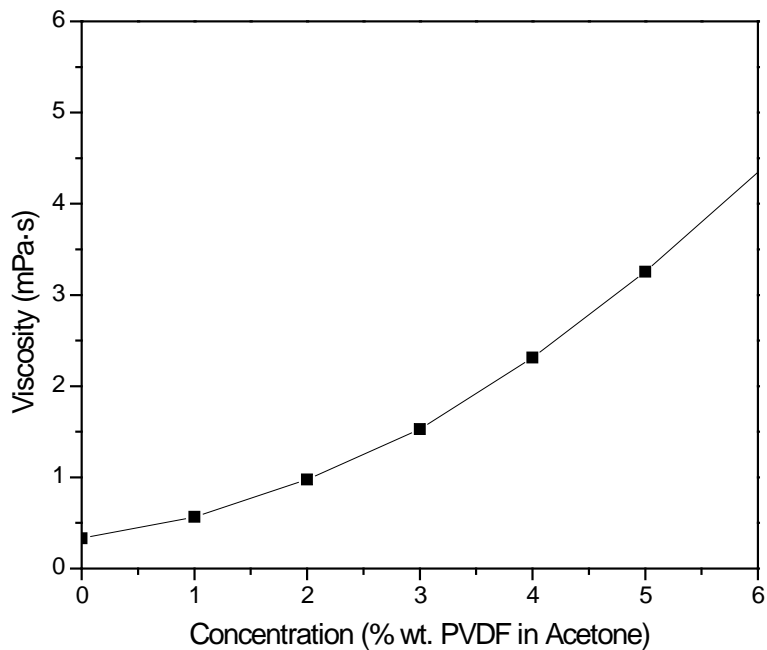


Figure 9: Viscosity vs. Concentration

Table 2: Spin Coating Conditions

Sample	Solution	Phase I		Phase II	
		Time (second)	Speed (RPM)	Time (second)	Speed (RPM)
A	3% wt. PVDF in acetone	5	500	45	1000
B	4% wt. PVDF in acetone	5	500	45	1000
C	5% wt. PVDF in acetone	5	500	45	1000

Prior to run the spin coater, a piece of blue tape was cut to fit the size of the substrate to be coated. The substrate was placed on the adhesive side of the blue tape. The other side of the blue tape was sucked by the vacuum chuck to secure the substrate on the center of the vacuum chuck. The solution was then dispensed from glass syringe onto the substrate carefully. Initially, the substrate spun at the speed and the time period pre-set for phase I to spread out the solution evenly across the substrate. After low speed spinning, it accelerated to spin at pre-set speed and time period for phase II to coat the substrate uniformly. The sample was then removed from vacuum chuck after the spinning stopped automatically.

2.2.2 Electrospray

Electrospray (ES) is a liquid atomization method that attracts growing interest in the aerosol community, mainly because of the phenomenal size range of particles it can

produce, from molecular dimensions to hundreds of microns. A typical ES system can be readily implemented by feeding a liquid with sufficient electric conductivity through a small capillary, which is charged to a high potential relative to a nearby ground electrode as shown by Figure 10.

Depending on the operating conditions and liquid property, the liquid at the nozzle tip can be atomized in several different operation modes. Zeleny did the first systematic study on those modes (Zeleny, 1917) and later Cloupeau and Prunet-Foch did a comprehensive phenomenological review (Cloupeau & Prunet-Foch, 1990). Among those modes, the most remarkable, widely used, and extensively studied is the *cone-jet* mode (Cloupeau & Prunet-Foch, 1990). In this mode, the liquid meniscus takes a conical shape, named Taylor-cone (Taylor, 1964), which is formed through a delicate balance between surface tension and normal electric stress at the liquid-air interface (Figure 10).

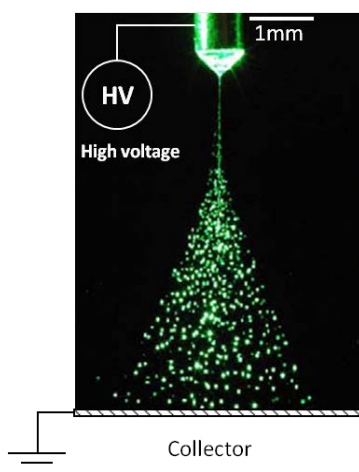


Figure 10: Typical Electrospay

The key features that distinguish *cone-jet* electrospray from other atomization methods are:

(i) Quasi-monodispersity: The *cone-jet* mode offers the appealing feature of droplet monodispersity (Chen, Pui, & Kaufman, 1995; Tang & Gomez, 1994). Typical relative standard deviation of the droplet diameter for the *cone-jet* ES is 10% or less. The quasi-monodispersity brings great convenience in fundamental study, because a single ES or even a single droplet can reveal valid information for theoretical analysis or numerical simulation. The uniform droplet size also makes the creation of homogeneous, ordered, or periodic structures possible. From a thin film perspective, uniform droplet size is also attractive to enable uniform mass and heat flux upon interaction of the droplet with the substrate, in turn generating higher quality thin films. The generated droplets can be categorized as two kinds according to their size: primary droplets and satellite droplets. Due to higher charge to mass ratio and larger initial velocity, the satellite droplets are always at the outer edge of spray profile and shroud the primary droplets, we can thus use an electrode with size controllable hole to block the satellite droplets only and realize better monodispersity (Hong, Li, Yin, Li, & Zou, 2008).

(ii) Tunable droplet and particle size in a wide range: From the *cone-jet* electrospray source, the droplet size can be controlled from nanometers to hundreds of micrometers continuously by either changing the liquid flow rate or adjusting the liquid conductivity. There are scaling laws (De La Mora & Loscertales, 1994; Higuera, 2003)

which relate the droplet size to these parameters. This allows us to tailor the droplet size which may be essential in applications which requires stringent droplet size distribution. In nanomanufacturing, a controlled and narrow distribution of size in the nanometric range is produced by dissolving a nonvolatile solute into an electrosprayable solvent to inhibit the rapid evaporation and eventual disintegration of the droplet. In spray drying, the final particle size can be further adjusted by the solute concentration. The size of the final solid particle product scale with $\eta^{1/3}d$, where η is the concentration of the precursor solution and d is the initial diameter of the liquid droplet. Therefore, low concentration, combined with small droplet size, may lead to very fine particles down to nanometer range.

(iii) Spray self-dispersion: Due to the same polarity of charge obtained from the power supply, the droplets repel each other under the Coulombic force, which prevents droplet coalescence and provides a way to manipulate the droplets through external electric field (Cha, Blades, & Douglas, 2000).

(iv) Dramatically reduced process time: Since the diffusion time for heat, mass and momentum, as well as the evaporation time, scales with d^2 , a small decrease in droplet diameter leads to dramatic reductions in the characteristic time. Short heat diffusion time suggests fast and precise regulation of droplet temperature, which is crucial during thin film fabrication processes. Reduced mass and viscous diffusion time makes quick mixing of reactants possible. For heat-sensitive materials, as in OPVs, it is

possible to have a reasonably fast evaporation even at modest temperatures, which avoids thermal destruction to the material.

(v) Low risk of clogging: The liquid being sprayed is fed into a relatively larger orifice (10^2 - $10^3\mu\text{m}$) compared to that in inkjet printing ($\sim 30\mu\text{m}$). The use of large bore minimizes the risk of liquid line obstruction and reduces pressure drop in the orifice.

(vi) Improved deposition efficiency due to image force: When electrically charged droplet approaches a conducting surface, an image charge is induced, generating an additional Coulombic force which tends to prevent droplet rebound from the substrate (Deng & Gomez, 2010). This mechanism can even eliminate the need for carrier gas since the charged droplet can be guided solely through electric field manipulation. This results in less material waste, and thus negative environmental impacts related to material waste is minimized.

Figure 11 shows a typical electrospray setup we used for both wet deposition and dry deposition. This experimental setup consists of five major components: a MRI Compatible syringe pump, a HAMILTON 100 μl syringe with 23s-26s gauge small hub removable needle, a cleaned substrate on motorized stage, high voltage source, and a digital camera with specialty lens. The x-y motorized stage is driven by stepper motors, and the axis of the x-y table moves at an adjustable speed of 36-174 mm/min with a resolution of 2 μm . The spraying paths were initially sketched on CAD software (Solid Works), and then converted into G-code, which could be adopted by the stepper motor controller. The most important criterion distinguishing the dry deposition and wet

deposition is the distance between the syringe needle and the substrate. For the dry deposition, the distance between the syringe needle and the substrate was 5cm, however, the distance between the syringe needle and the substrate was about 3-4 mm in wet deposition.

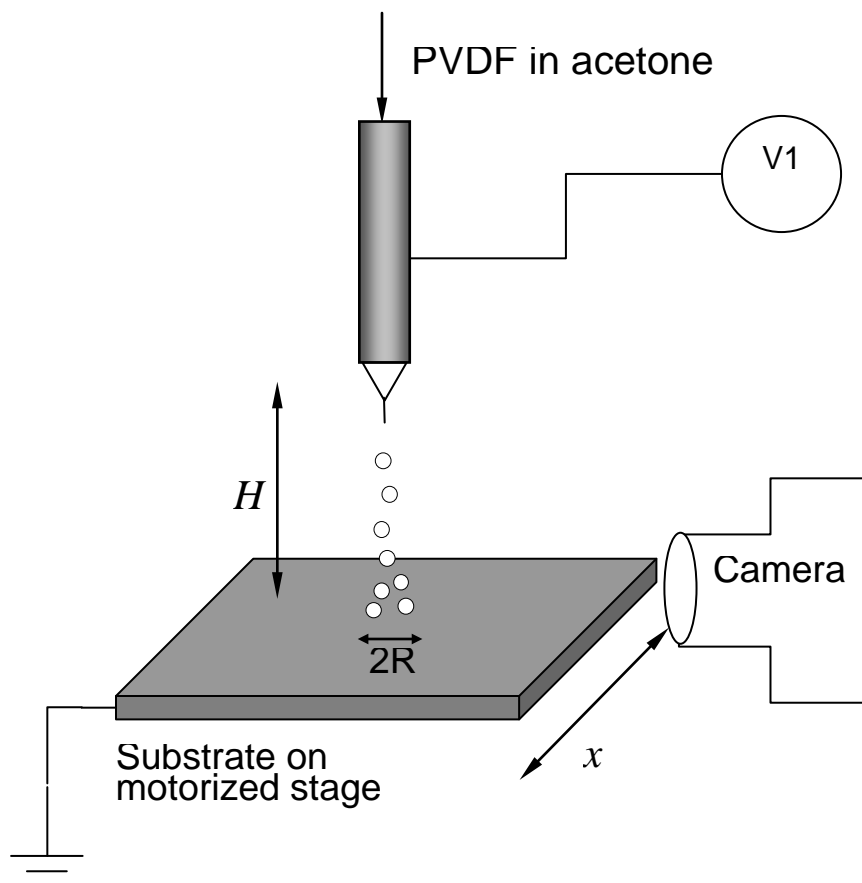


Figure 11: (a) The ES as a printing head, with near-field and far-field schematically illustrated. (b) ES printing setup

Dry Deposition

The 2% wt. PVDF in acetone solution was electrosprayed through the syringe needle at flow rate of 0.8, 3, and 5 $\mu\text{l}/\text{min}$ onto a substrate. The cone-jet mode electrospray was initially observed and verified using the camera system before beginning the substrate motion. The substrate moved at a constant speed of 75 cm/min over the deposition area. In order to produce a 5 μm thick film, the substrate was moved back and forth along x-axis for 375, 100, and 60 times corresponding to the flow rate of 0.8, 3, and 5 $\mu\text{l}/\text{min}$. For the dry deposition experiments, the solution concentrations, flow rates, and number of the passes were changed correspondingly to each other to control the thickness of the films to be constant. A summary of the dry deposition conditions for the nine experiments are given in Table 3.

Table 3: Dry Deposition Conditions

Sample	Solution Concentration	Flow Rate ($\mu\text{l}/\text{min}$)	Number of Passes
D2A	2% wt. PVDF in Acetone	0.8	375
D2B		3	100
D2C		5	60
D3A	3% wt. PVDF in Acetone	0.8	250
D3B		3	67
D3C		5	40
D4A	4% wt. PVDF in Acetone	0.8	188
D4B		3	50
D4C		5	30

Wet Deposition

Two sets of experiments were conducted for the wet deposition experiments. The PVDF in acetone solution was electrosprayed through the syringe needle at flow rate of 5, 10, and 15 $\mu\text{l}/\text{min}$ onto a substrate. The cone-jet mode electrospray was initially observed and verified using the camera system before beginning the substrate motion. The substrate moved at a constant speed of 174 mm/min over the deposition area. The substrate moving speed was kept constant, while the solution concentrations and flow

rates were varied. A summary of the wet deposition conditions for the nine experiments are provided in Table 4.

Table 4 : Wet Deposition Conditions with Different Parameters

Sample	Solution Concentration	Flow Rate ($\mu\text{l}/\text{min}$)
W2A	3% wt. PVDF in Acetone	5
W2B		10
W2C		15
W3A	4% wt. PVDF in Acetone	5
W3B		10
W3C		15
W4A	5% wt. PVDF in Acetone	5
W4B		10
W4C		15

The purpose of carrying first set of experiment was to reproduce the same porous structure obtained from the spin coating. The samples were examined and the porous structures were confirmed under the scanning electrons microscopy (SEM). The objective of the second set of experiments was to characterize the relationship between

the pore sizes, pore density, and the thickness. A summary of the wet deposition conditions for the five experiments are presented in Table 5.

Table 5: Wet Deposition Conditions with Different Substrate-Moving Speed

Sample	Solution Concentration	Flow Rate ($\mu\text{l}/\text{min}$)	Substrate Moving Speed (mm/s)
W45A	4% wt. PVDF in Acetone	5	36.25
W45B			73.95
W45C			110.20
W45D			146.45
W45E			174

2.3 Spray Characterization

Phase Doppler Interferometry is a modest, laser based diagnostic technique for measuring droplet size and velocity. In 1980, Bachlo (Artium's founder) theoretically described light scattering from spherical particles and showed that the phase shift of the light scattered from two intersecting beams could reliably measure the diameter of spherical particles. The technique has since evolved as the standard laser-based diagnostic instrument for simultaneously measuring the size and velocity of individual spherical particles. In this work, we used an advanced 'self contained' PDI. A self contained unit is essentially a single box which houses all of the optic components. Heritage PDI systems require manual setup and alignment of all of these components on an optical table, which can consume a considerable amount of time to setup and maintain. Refer to Figure 12 for a schematic of typical PDI system components.

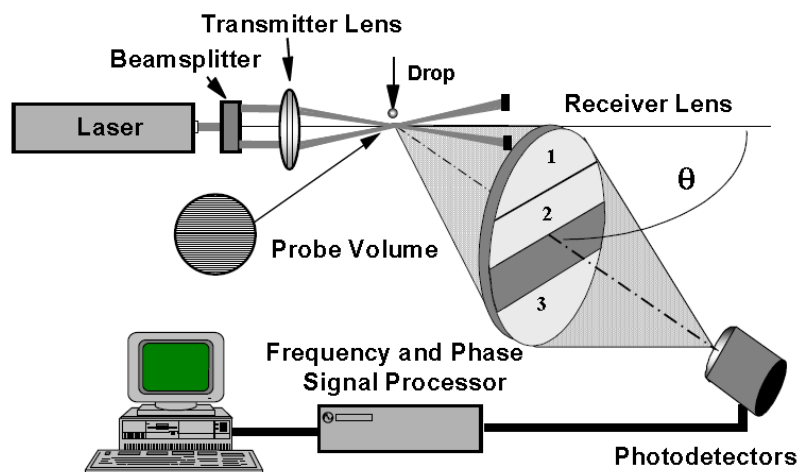


Figure 12: Typical PDI setup and system components

In summary, the PDI uses a monochrome laser (diode pumped solid-state 532nm) in conjunction with a beam splitter to divide the initial laser beam into two beams of equal intensity and wavelength. These two beams are then sent through a series of lenses and mirrors and out of a window at an approximate 7° angle. The beams then intersect at the probe volume, where a fringe pattern will appear due to the interference of the two beams. The fringe spacing is proportional to the laser wavelength over the sine of the beam intersection angle. The well-defined fringe pattern becomes the basis for interrogating droplets. Refer to Figure 13 top-left for an illustration of beam splitting and resulting fringe pattern.

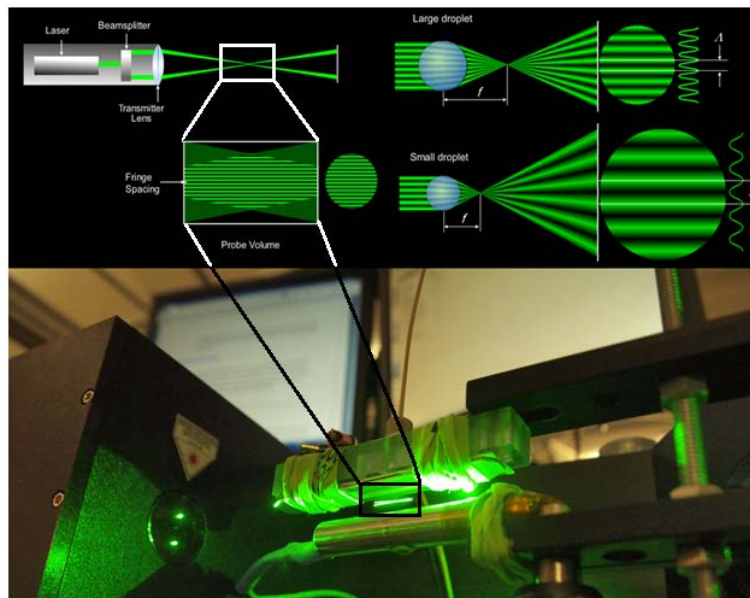


Figure 13: Top - Schematic of PDI Principle, Bottom - Early generation 15 nozzle device in the PDI, notice the subtle crossing of the two beams in the spray cloud.

Droplets are then brought to pass through the probe volume with some velocity. Each droplet acts like a lens, refracting the incident light at an angle dependent upon its

curvature, i.e. its diameter. More specifically, the passing droplets refract and magnify the interference fringes in the probe volume. Smaller droplets with larger curvature diverge and magnify the fringes more than large droplets with intrinsically smaller curvature. Refer to Figure 13 Top right for an illustration of the magnifying lens effect of small versus large diameter droplets. The refracted fringe pattern is then collected by a series of photodetectors placed at calibrated spacing. For a single droplet, the signals on each photodetector are identical in frequency and amplitude, but with a slight shift in the signal's time signature (phase) due to the distance between photodetectors. This phase shift is proportional to the size of the droplet, while the signal's frequency is used to derive the droplet velocity. Figure 14 shows the experimental result of droplet size respect to the flow rate of pure acetone.

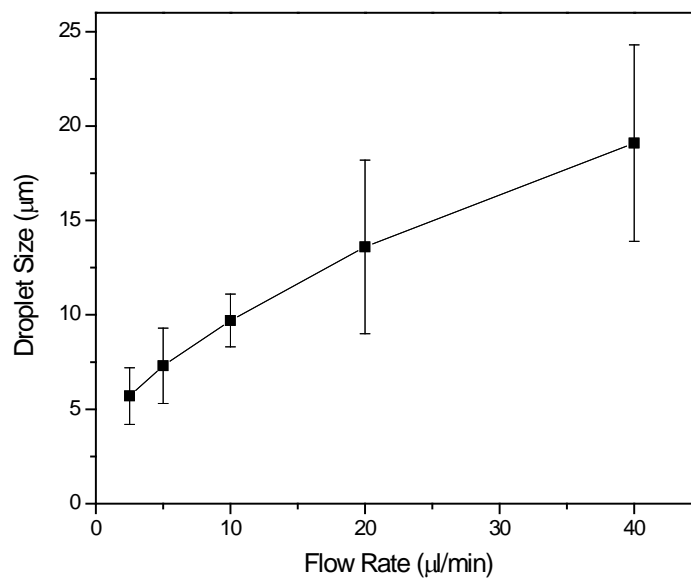


Figure 14: Droplet Size vs. Flow Rate

CHAPTER 3: RESULTS AND DISCUSSION

3.1 Dry Deposition

3.1.1 *Rayleigh instability and Coulombic fission*

As the uniform and stable electrospray droplet flights towards the substrate, it evaporates and shrinks. When its charge density reached to a certain point, this droplet becomes unstable and its charge moves towards the surface of the droplet. If the surface charge density is adequately high, the Coulomb repulsion among charges will overcome the binding effect of the surface tension. As a result, the droplet becomes instable and disrupts. This process is known as Coulomb fission. Rayleigh devoted his time into the critical condition for the radius instability of a spherical droplet, R , and he was able to computed the maximum charge of an isolated droplet with uniform distribution of charge in its surface could hold before the instability occurs, which is nowadays known as the Rayleigh limit q_R ,

$$q_R = 8\pi(\epsilon_g \epsilon_0 \gamma R^3)^{1/2}$$

The radius of the droplet when it reaches the Rayleigh limit for a certain charge q can be derived from this equation, and is equal to

$$R_R = \left(\frac{q^2}{\pi^2 64 \epsilon_g \epsilon_0 \gamma} \right)^{1/3}$$

When the Rayleigh instability is reached, the surface of the droplet becomes unstable and disrupts. As a result, it ejects a fine spray similar to that emitted from a Taylor cone. The offspring droplets ejected normally compose 1-2% of the mass of the original droplet and 15% of its charge (Gomez & Tang, 1994). The droplet becomes stable again because the ejected offspring droplets are highly charged. Figure 15 is captured by Gomez and Tang. It shows the electrospray droplets undergoing Coulomb fissions in flight.

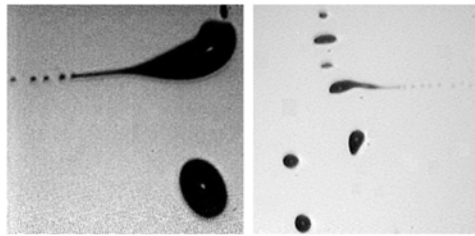


Figure 15: Flash-shadowgraphs of electrospray droplets undergoing Coulomb fissions in flight (adopted from (Gomez and Tang 1994))

Rayleigh instability sets in again and again for both parent and offspring droplets as the evaporation continues. Coulomb fission is repeated until the droplet is sufficiently "solid" to prevent the fission or the neutralization of the droplet occurs when it reaches the grounded collector, whichever happens first. (Almería-Díez, 2012)

3.1.2 Spray drying mechanism

Figure 16 shows diverse morphologies obtained in PLGA particles as a result of Coulomb fissions in the precursor droplets (adopted from Almería-Díez, 2012). The

morphologies includes spherical (Figure 16a), elongated (Figure 16b) and complex shaped particles with one (Figures 16c and 16d) or multiple (Figure 16e) fibers emerging from the particle.

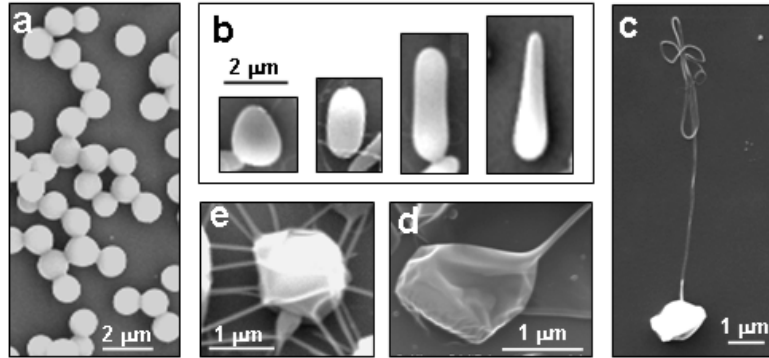


Figure 16: Diverse morphologies obtained in PLGA particles as a result of Coulomb fissions in the precursor droplets. (adopted from Almería-Díez, 2012)

Figure 17 and 18 summarizes these processes as the outcome of two possible scenarios for the evolution of a charged droplet of a dilute polymer solution undergoing solvent evaporation. Figure 17 and 18 Entanglement effects on particle morphology in the context of Coulomb fission.

The relative magnitude of the polymer volume fraction in a droplet at the Rayleigh limit, ϕ_{Ray} , the overlap volume fraction, $\phi_{\text{ch.ov}}$, and the entanglement volume fraction, ϕ_{ent} , determine the different outcomes that Coulomb fission and chain entanglements can yield. If $\phi_{\text{Ray}} < \phi_{\text{ch.ov}} < \phi_{\text{ent}}$, the droplet is still adequately dilute to behave like a pure solvent (Figure 17). In this circumstance, the droplet ejects small yet highly charged offspring droplets during Coulomb fission.

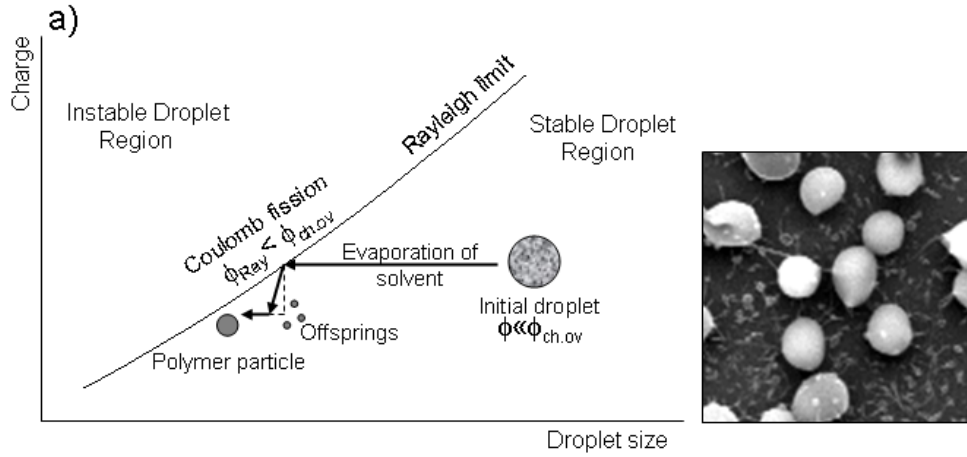


Figure 17: Particle Morphology (a)

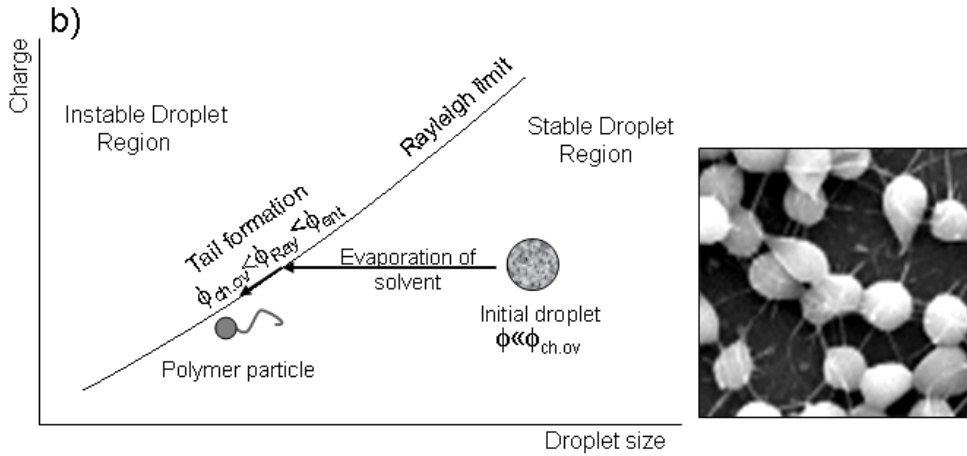


Figure 18: Particle Morphology (b)

The other scenario is when $\phi_{ch.ov} < \phi_{Ray} < \phi_{ent}$ (Figure 18), the particle is not strong enough from deforming during the Coulomb fission, though sufficiently strong to preserve the droplet integrity. Consequently, the particle ejects a thin and long charged fiber and deforms. The SEM micrographs suggests that it remains frozen in that shape because the evaporation process is nearly complete. It is generated when the Rayleigh

limit is reached at a late stage in the evaporation process, which “freezes” the stretched particle morphology before the ejection of mass. Depending on the extent of stretching reached by the droplet before complete evaporation, particles with different aspect ratio can be obtained.

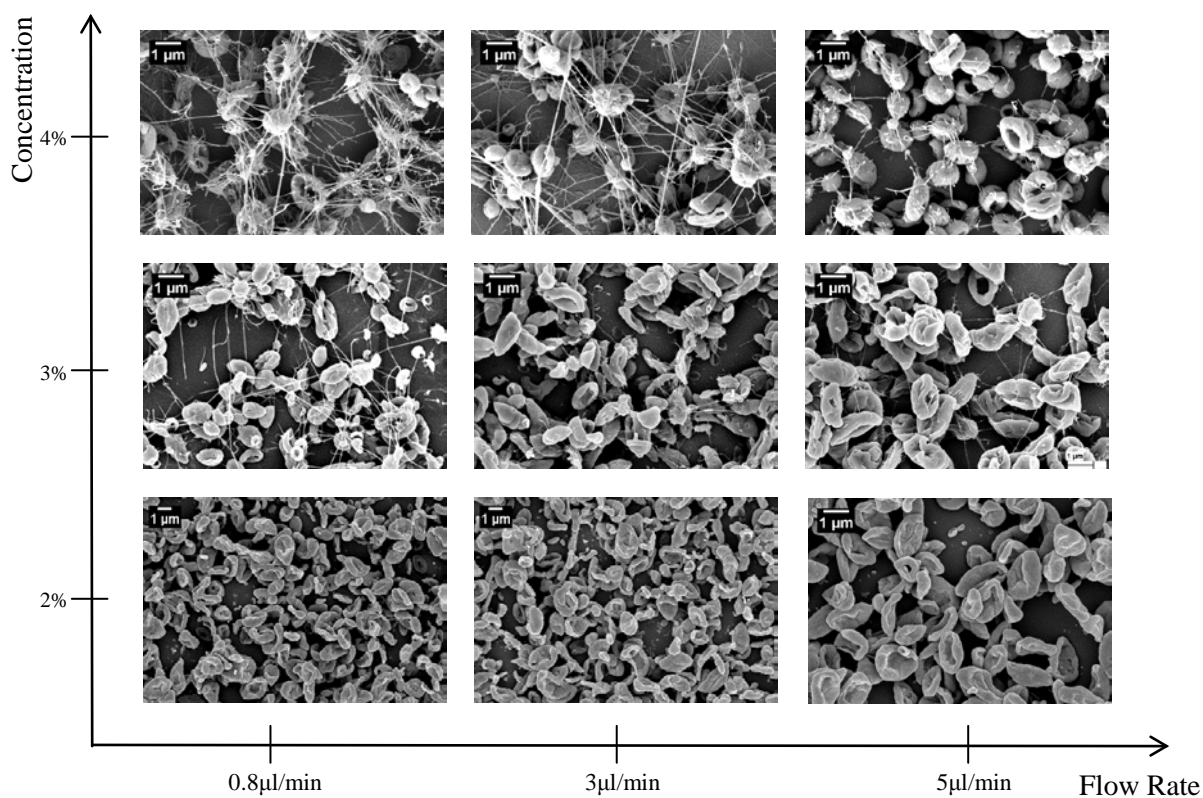


Figure 19: Overview of PVDF particles synthesized with Acetone, for different solution concentration and solution flow rates.

Figure 19 displays the PVDF particles synthesized with acetone as the ES solvent observed under scanning electron microscope (SEM) with different concentration and flow rate. Figure 19 suggests that the morphology of the synthesized PVDF particles depends on both flow rate and solution concentration. In conclusion, we

discover that higher solution concentrations have a tendency for preserving spherical particle. On the other hand, larger flow rates are in favor of synthesizing more complex particles. These results can also be generalized to other combinations of solvent and polymer.

3.1.3 The effect of film morphology to contact angle

In order to create superoleophobic surface; theoretically, the surface energy of the material has to be lower than any of known materials. Therefore, Tuteja et al introduced the third criterion, re-entrant surface curvature. The re-entrant curvature of a surface is the area that curves under a fiber as it sits atop a mesh of other fibers, which exhibits highly resistance to wetting from several low surface tension liquids with chemical composition and roughened texture (Pan et al., 2013).

Wenzel State

Wenzel model (Figure 20) can only describe the homogeneous wetting regime, however, the Cassie model is more sufficient to deal with heterogeneous surface. Wenzel model express the apparent contact angle respect to surface roughness and the equilibrium contact angle as:

$$\cos\theta^* = r\cos\theta$$

where θ^* =the apparent contact angle on the textured surface

r = the surface roughness

θ = the equilibrium contact angle on a smooth surface of the same material.

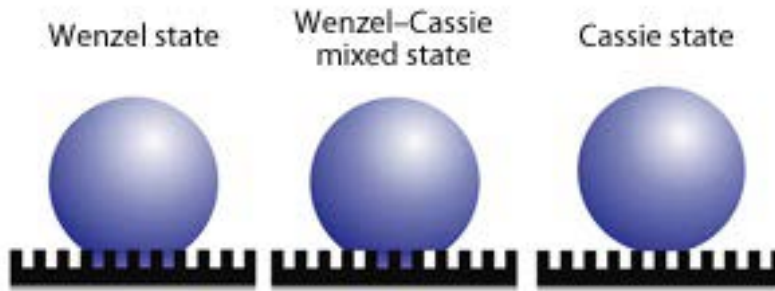


Figure 20: Different States of Superhydrophobicity

Cassie State


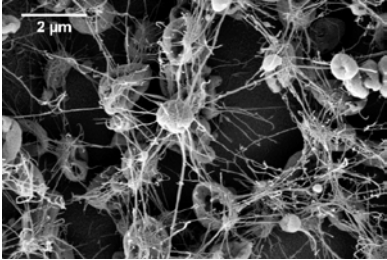

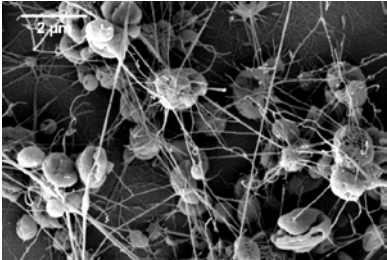

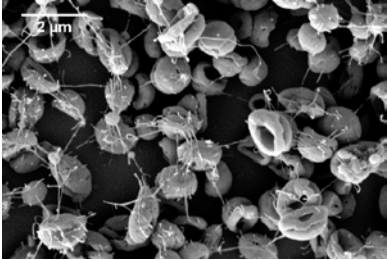
In contrast, the Cassie model (Figure 20) explain that the superhydrophobic nature of a rough surface is caused by microscopic pockets of air remaining trapped below the liquid droplet, leading to a composite interface. The Cassie equation yields:

$$\cos\theta^* = -1 + \phi_s(1 + \cos\theta)$$

Where ϕ_s = the fraction of the solid in contact with the liquid.

Table 6 suggests that these PVDF particles and fibers function as re-entrance surface. The surfaces covered by PVDF particles and fibers exhibit highly water-repelling properties, which indicates its ability of supporting the Cassie state with water. In addition, the Cassie state is accessible in practice even if the pressure is applied. The presence of re-entrant curvature constructed with the water repelling properties of PVDF is satisfied for developing highly non-wetting surfaces.

Table 6: Deposition and Particle Phenomenology with different Flow Rate

Sample	Solution Concentration	Flow Rate ($\mu\text{l}/\text{min}$)	Contact Angle	SEM
D4A	4% wt. PVDF in acetone	0.8	 $\theta=157^\circ$	
D4B		3	 $\theta=152^\circ$	
D4C		5	 $\theta=146^\circ$	

3.2 Wet Deposition

3.2.1 Honeycomb morphology

Figure 21 exhibits the PVDF film observed under scanning electron microscope (SEM). After we had discovered these uniform hexagonal porous structures, we sought the theory underlying these porous structures. In this section, we will discuss and examine all the possible theories.

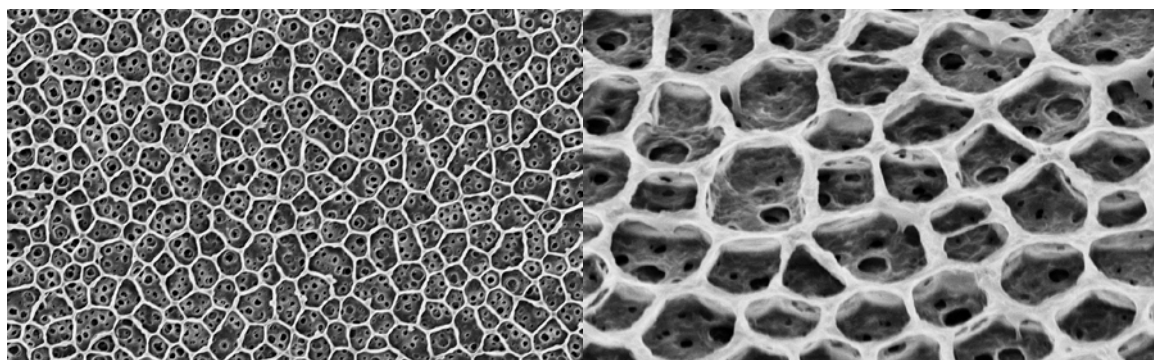


Figure 21: SEM micrograph of PVDF film

Theory one: Breath Figure

The concept of breath figure is to condense water droplets on the surface of a solution, draw them beneath the surface, and then evaporate all the solvent and water to reveal a highly porous microstructure. Figure 22A establishes the set up for the phenomenon. Very humid air floods a polymer dissolved in a volatile solvent. As the solvent evaporates, the surface becomes cold. In Figure 22B, we see that the temperature difference causes condensation of water droplets on the solution surface.

As the process continues, these droplets become larger (Figure 22C) until their mass is sufficient to allow them to sink (Figure 22D). It becomes fairly obvious that the solvent must be immiscible with water and less dense. Once the layer of droplets has submerged, the process may begin again with a new set of droplets (Figure 22E and F) until a three dimensional ordered arrangement of droplets exists throughout the film (Figure 22G). Figure 22H demonstrates how the polymer dries around the spherical droplets to cover them while remaining ordered. The surface has been removed on the portion of figure H where the struts seem thin. Figure I demonstrates the 3d capacity of the breath figure such that when a cross section is taken, voids may be observed all the way through (even if the soft polymer was distorted by the slicing process). (Ding et al., 2013)

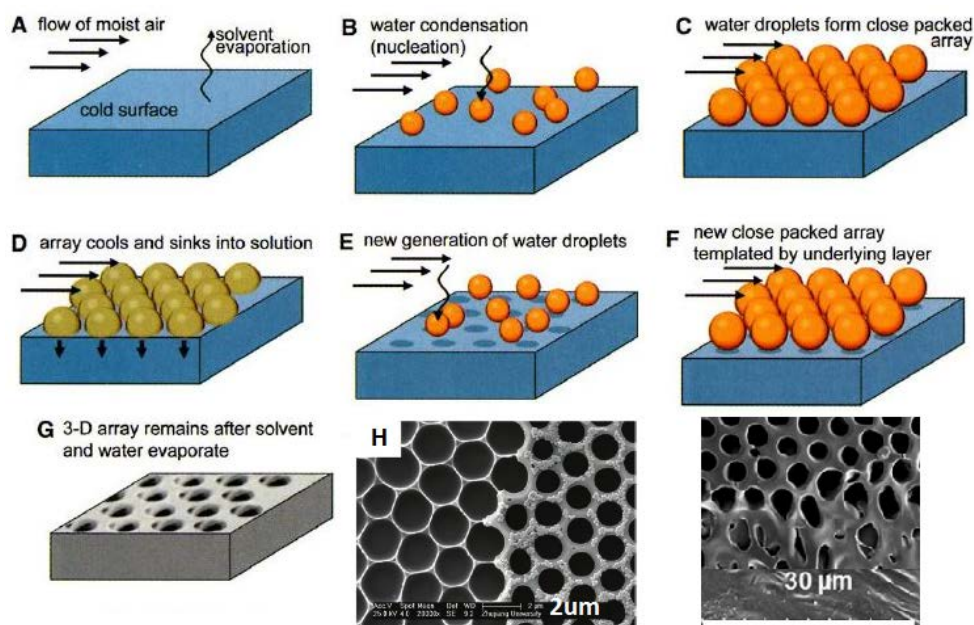


Figure 22: Breath Figure Method (adopted from A-G: Srinivasarao et. al, 2001 ; H: Ke, Wan, et. al, 2010; I: Ponnusamy et. al, 2012)

Theory two: Bernard type of flow instabilities

Rayleigh-Bénard

Rayleigh–Bénard convection is one type of natural convections. It occurs when a thick layer (minimum thickness=1mm) of fluid is heated from below, which leads a density gradient between the top and the bottom boundaries of the fluid. As a result, the gravity causes the cooler and denser fluid falling from the top to the bottom. This gravitational force acts against to the viscous force within the fluid. Rayleigh number was then introduced to explain the relationship between these two forces. From equation 1, we can tell that if the temperature of the bottom boundary increases while all the other parameters stay same, then the Rayleigh number will increase. (Shan, 1997)

$$Ra_L = \frac{g\beta}{\nu\alpha} (T_{bottom} - T_{top})L^3$$

T_{top} =the Temperature of the top plate

T_{bottom} =the Temperature of the bottom plate

L =the thickness of the fluid.

g =the acceleration due to gravity.

ν =the kinematic viscosity.

α is the Thermal diffusivity

β is the Thermal expansion coefficient

When it reaches the critical Rayleigh number, the instability takes places, which the gravitational forces dominate the convention and a regular pattern of convection

cells are developed by fluid. If the temperature of the bottom boundary further increases, the structure would become more complex with the turbulent flow involved. The critical Rayleigh number is determined by boundary condition. It can be obtained analytically from the linearized equations in the stable state. In our case, the critical Rayleigh number comes out as $R_c = 1,100.65$. The shape of each individual Bénard cell looks like regular hexagonal prisms, particularly in the absence of turbulence, although certain experimental conditions can result in the formation of regular right square prisms or spirals. Figure 23 a and b show the Rayleigh–Bénard convection happened in nature.



(a) (b)
Figure 23: Natural Rayleigh–Bénard Convection

Bénard–Marangoni

Bénard–Marangoni convection is a specific case of Rayleigh–Bénard convection. It is known as temperature gradient-driven surface tension variations. In this case, the thickness of the fluid is less than 1 mm; therefore, surface tension effects will be more dominant in how the convection patterns develop. According to Marangoni effect, fluids

tend to flow from area of lower surface tension to area of higher surface tension. When a horizontal layer of the fluid is heated from below, temperature instabilities appear on the top layer of the fluid. As temperature increases, surface tension decreases. A lateral flow of fluid at the surface will set in and move from warmer areas to cooler areas. In order to maintain a horizontal fluid surface, cooler surface fluids will descend, which provides the driving force of the convection cells. (Semwogerere & Schatz, 2004)

Gibbs-Marangoni

The Gibbs-Marangoni convection is a specific case of Bénard–Marangoni convection. It is known as the mass gradient-driven surface tension variations. In this case, the thickness of the fluid is so small that the fluids will be considered as isothermal system. Therefore, Bénard–Marangoni convection driven by temperature difference will not happen in this case. Surface tension effects, which are driven by concentration difference, will be more dominant in how the convection patterns develop.

As the solvents evaporate, the fluids at the surface become denser than the fluids underneath it. Surface tension increases while concentration increasing. According to Marangoni effect, fluids tend to flow from area of lower surface tension to area of higher surface tension. A lateral flow of fluid at the bottom will move from more dilutive areas to denser areas. In order to maintain a horizontal fluid surface, denser fluids will descend, which provides the driving force of the convection cells. Due to the large molecular weight of the PVDF, which leads to high molecular concentrations of the solutions, the Gibbs-Marangoni effects are strong in our case.

Mathematic model

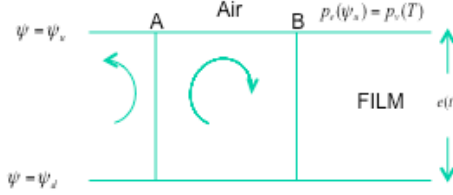


Figure 24: A solvent-rich fluctuation rises and lowers the surface tension at point A. Thus the fluid is driven from A to B and the fluctuation is amplified. (adopted from Gennes, 2001)

In order to describe Gibbs-Marangoni effect mathematically, we assume that a roll instability is superposed on the diffusion flux. As the solvent evaporates, a significant difference is perceived between the solvent fractions ψ_d at the bottom and the solvent fractions ψ_u at the free surface. As a result, a concentration difference is induced between point A (ψ_A) and point B (ψ_B) (Figure 24). This difference can be estimated by balancing the convection and diffusion:

$$D_{coop} \frac{\psi_A - \psi_B}{e} \cong V(\psi_d - \psi_u) \quad (1)$$

where V = the convective velocity

$$\psi_A - \psi_B = \text{solvent concentration difference}$$

In general, the mass transfer through a boundary layer involves both diffusion and convection. In our case, we describe both of them as diffusion due to the fixed thickness l (~ 1 mm) and eliminate the noise in the experiment. The diffusion within the film is:

$$W = D_{coop} \frac{\psi_d - \psi_u}{a^3 e} \quad (2)$$

where D_{coop} = the cooperative diffusion coefficient of the solution

a = the size of a solvent molecule

The diffusion above the free surface is:

$$W = D_{air} \frac{\gamma G(e) - \gamma G(e+l)}{l} \quad (3)$$

According to ideal gas law, the number of solvent molecules in the gas per unit length $\gamma G(z)$ decreases linearly respect to p_v :

$$\gamma G(z = e) = \frac{p_v}{KT} \quad (4)$$

Assume there are no solvent molecules at the boundary layer, the number density of solvent molecules at the boundary layer equals to:

$$\gamma G(z = e + \ell) = \frac{p_v}{KT} = 0 \quad (5)$$

By substituting Equation (5) into Equation (3), the mass flux above the free surface can be simplified as:

$$W = D_{air} \frac{\gamma G(e)}{l} \quad (6)$$

The diffusion constant of solvent in air D_{air} is proportional to $v_{th}\lambda$, which gives:

$$D_{air} \cong \frac{v_{th}}{a^2} \frac{kT}{p_a} \quad (7)$$

where v_{th} = thermal velocity for a solvent molecular

λ = mean free path

a = the size of a solvent molecule

By substituting Equation (4), (6) and (7) into Equations (2), we derive and define the driving force for the convective instability as:

$$\psi_d - \psi_u \sim \frac{e}{l} \frac{av_{th}}{D_{coop}} \frac{p_v}{p_a} \quad (8)$$

Assuming $e = 1\mu$, $l = 1\text{mm}$, $av_{th} = 10^{-3} \text{ cm}^2/\text{s}$, $D_{coop} = 10^{-6} \text{ cm}^2/\text{s}$, and $p_v = 30\text{KPa}$, we get $\psi_d - \psi_u \sim 0.0003$.

The surface tension gradient induces by $\psi_A - \psi_B$ can be described as:

$$\nabla\gamma \cong \frac{\gamma_A - \gamma_B}{e} = \frac{-\gamma'_s}{e} (\psi_A - \psi_B) \quad (9)$$

Finally, V is defined by a balance between surface forces and viscous forces:

$$\nabla\gamma \sim \frac{\eta V}{e} \quad (10)$$

where η = the solution viscosity.

By merging Equation (2), (9) and (10), the critical thickness is:

$$e^* \cong \frac{\eta D_{coop}}{|\gamma'_s|(\psi_d - \psi_u)} \quad (11)$$

In the semi-dilute regime, D_{coop} is estimated to be:

$$D_{coop} = \frac{kT}{\eta_s \xi} \quad (12)$$

where kT = the thermal energy

η_s = the solvent viscosity

ξ = the mesh size in the solution

The result yields:

$$e^* \cong \frac{kT}{|\gamma'_s| \xi} \frac{\eta}{\eta_s (\psi_d - \psi_u)} \quad (13)$$

By substituting Equation (8) into Equations (13), we can derive that:

$$(e^*)^2 \sim \frac{kT}{|\gamma'|} \frac{l\eta}{\xi \eta_s} \frac{D_{coop} p_a}{av_{th} p_v} \quad (14)$$

we assume $|\gamma'| = 10\text{mJ}/\text{m}^2$, $\xi = 10\text{nm}$, $\eta/\eta_s = 10^6$, $l = 1\text{mm}$, and $D_{coop}/v_{th}a = 10^{-3}$, therefore, $e^* \sim 1 \mu\text{m}$. Equation (14) suggests that higher values of p_v lead to lower values of e^* ; the

instability (which occurs for $e > e^*$) is favored. (Gennes, 2001 & J.R.A. PEARSON, 1958)

3.2.2 *The effect of solvent volatility*

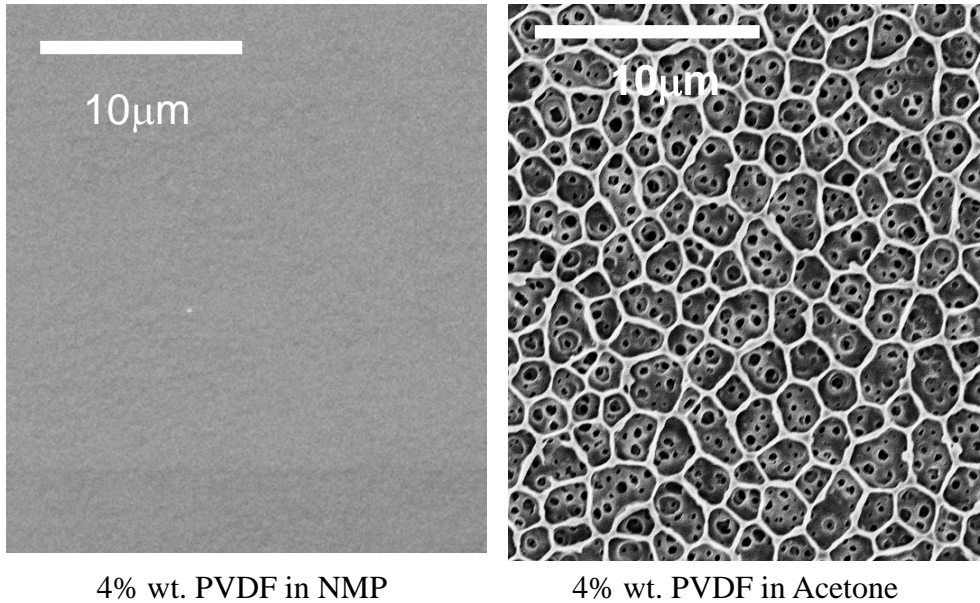


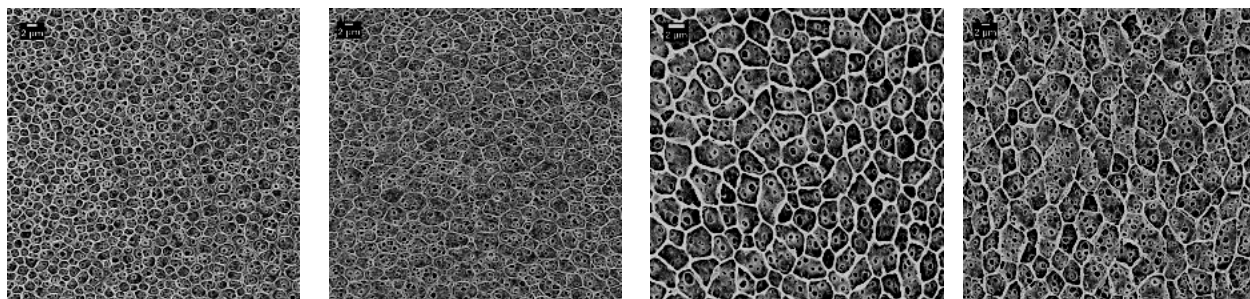
Figure 25: PVDF Films Synthesis with NMP and Acetone

Solvent volatility was found to affect the surface texture of PVDF film through its vapor pressure as we mentioned before in our mathematical approach. Figure 25 shows SEM micrographs of 4% wt. PVDF in NMP (Figure 25a) and 4% wt. PVDF in acetone (Figure 25b). Both samples are spin coated at 1000RPM. From our mathematical approach along with experimental results of two different solvents (Figure 25), we can conclude that the vapor pressure of the solvent has a huge impact on the structure of the PVDF film and determines the morphology of the PVDF film.

3.2.3 Control of the average pore size

The dependency of the pore size mainly on the thickness of the film indicates the possibility of producing a porous structures film with pore sizes as small as a few microns. The size of the pore can be controlled in three ways: either by varying the concentration of polymer in solution, or changing the solution flow rate, or adjusting substrate-moving speed since the thickness of the film varies monotonically with these three parameters. However, varying the concentration of the solution might result changes in more parameters, which could even lead to a change in morphology. Furthermore, the flow rate can only be changed within a certain range inside the ES stability domain. Therefore, the best way to investigate the relationship between the pore size and thickness is to adjust the substrate-moving speed.

Five samples at substrate-moving speed of 36.25, 73.95, 110.20, 146.45 and 174mm/min were electrosprayed. However, the sample at substrate-moving speed of 174mm/min was determined to be an outlier and therefore eliminated. The film thickness of the other four samples were calculated to be 22.07, 10.82, 7.26 and 5.46 μ m, respectively. Figure 26 shows the SEM micrographs of the samples. As we expected, the experimental result yielded that the size of the pores increases linearly with respect to the thickness of the film for all of the thicknesses studied here. (Figure 27) Also, as Figure 28 suggests that as the thickness increases, the pore density decreases.



(A)

(B)

(C)

(D)

Figure 26: SEM Micrographs of Samples with Thickness of 22.07, 10.82, 7.26 and 5.46 μm

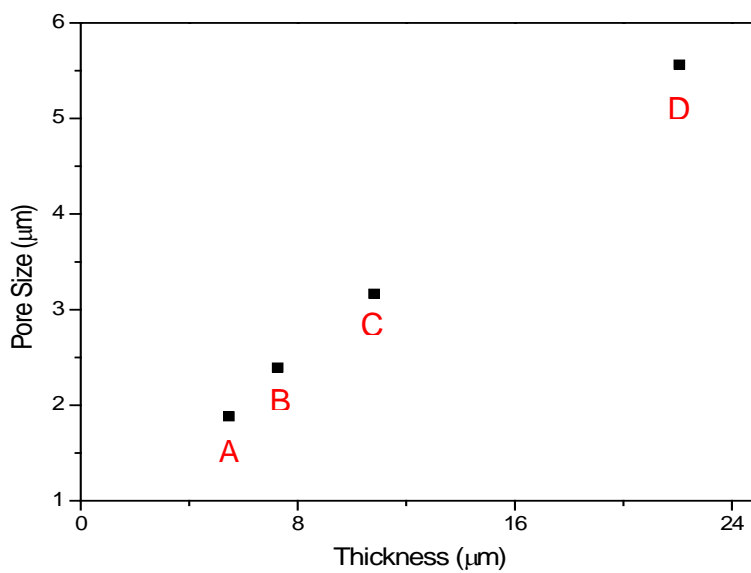


Figure 27: Pore Size vs. Thickness

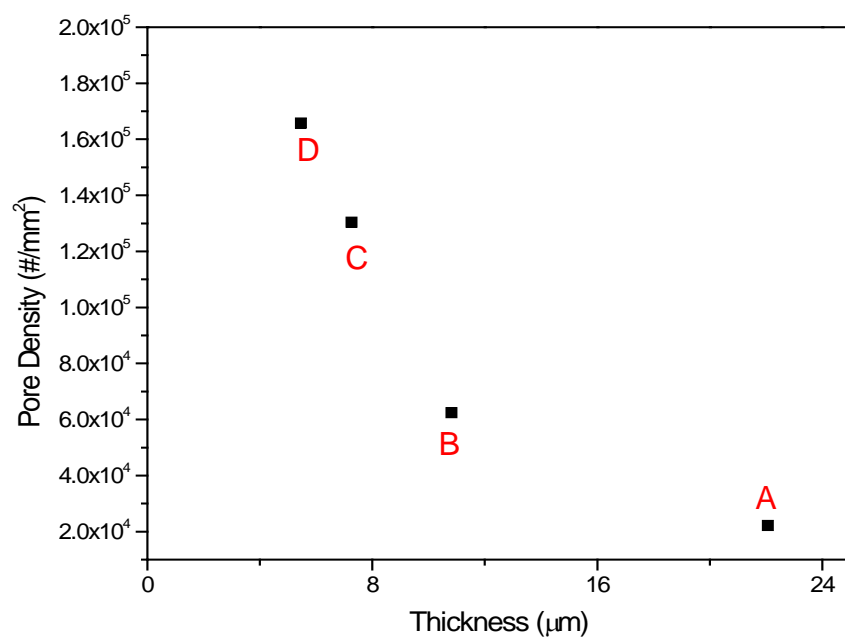


Figure 28: Pore Density vs. Thickness

3.2.4 Drag reduction of honeycomb texture

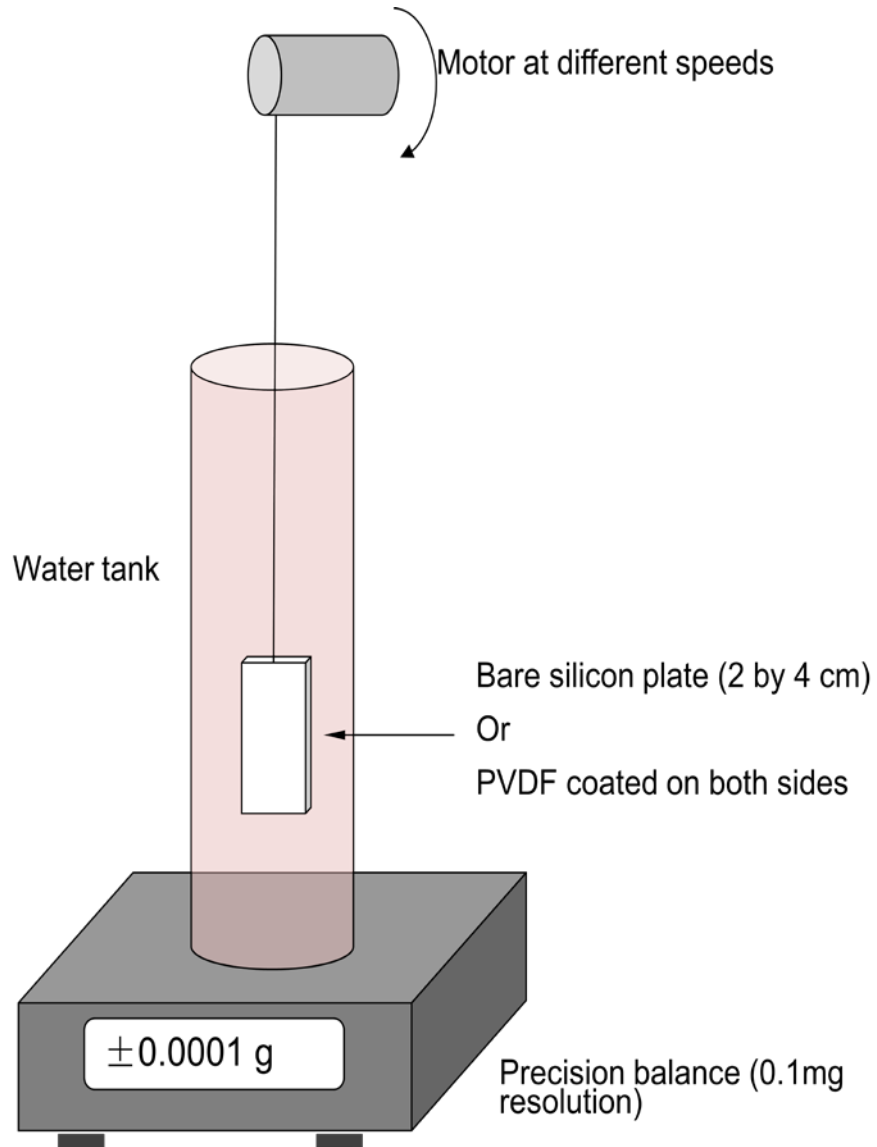


Figure 29: Experimental Setup for Drag Measurement

Figure 29 shows the experimental setup for drag measurement. In order to demonstrate the effect of our surface texture on drag reduction, the drags of the bare

silicon wafer and PVDF coated silicon wafer are measure multiples times at the different velocity. All experimental data are then organized and plotted in Figure 30 and 31.

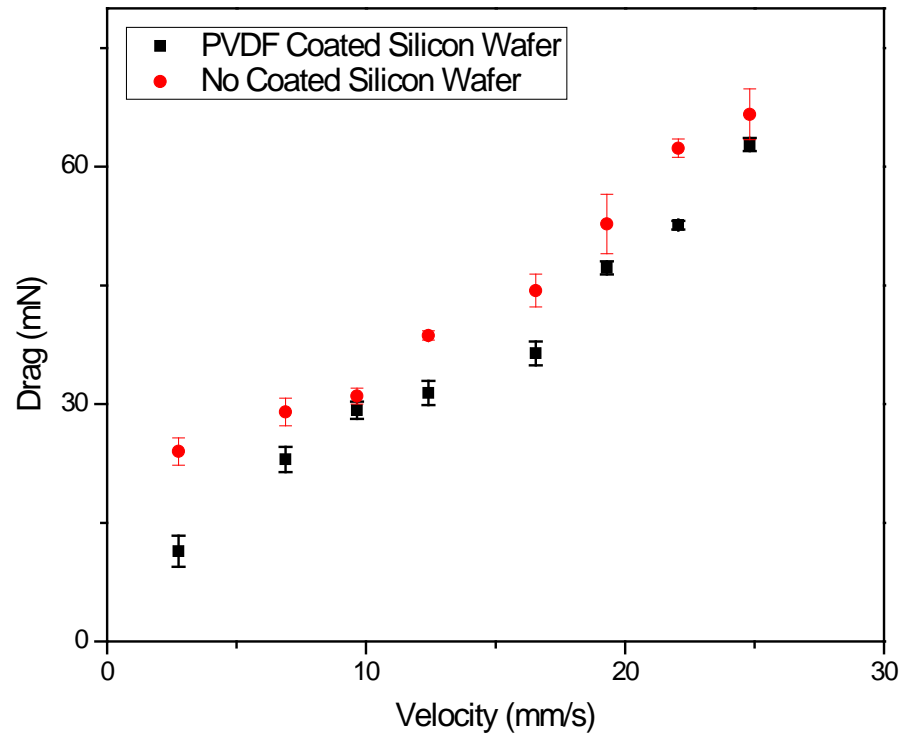


Figure 30: Drag vs. Velocity

Since drag depends on the flow in the boundary layer, we can predict some changes with surface roughness. It is observed experimentally that a coated silicon wafer will transition to turbulent flow at a lower speed than a clean silicon wafer. Drags for the coated silicon wafer at different speeds are shown on the Figure 29 in red dots, while the non-coating silicon wafer in black squares. The result yielded that there is a range of Reynolds numbers for which the drag of the coated silicon wafer is much less

than the drag of the smooth silicon wafer for the same surface area, velocity and flow conditions. Figure 30 shows the relationship between drag coefficient and Reynolds number for smooth silicon wafer and coated silicon wafer. At a lower Reynolds number, the drag coefficient of coated silicon wafer is much less than a clean silicon wafer.

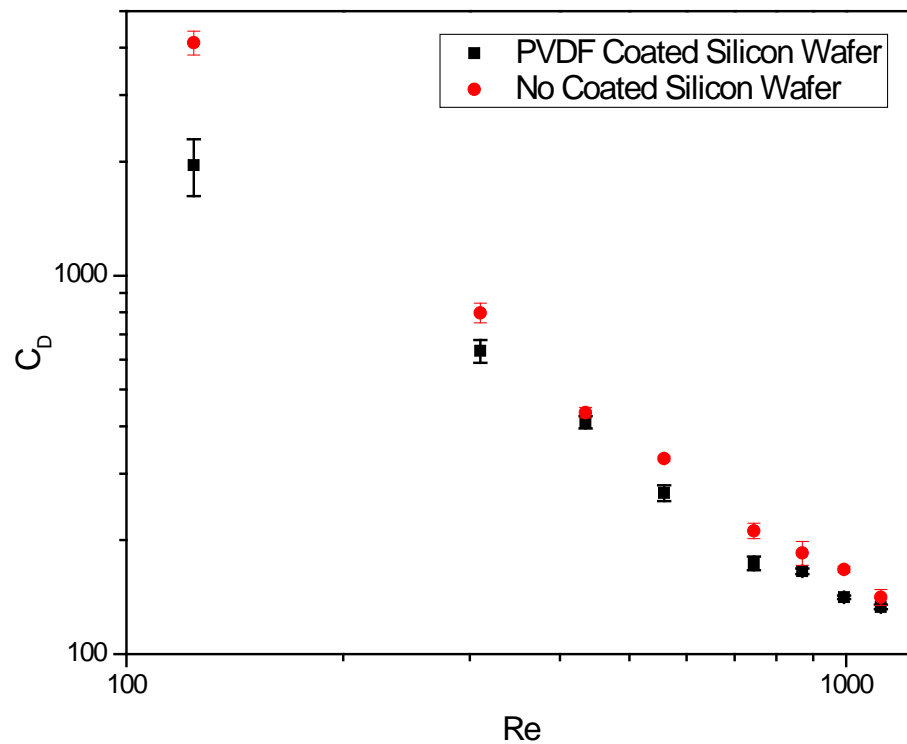


Figure 31: Drag Coefficient vs. Rayleigh Number

CHAPTER 4: CONCLUSIONS

In nature, microscopic surface textures exhibit some useful functions, for example, the drag reduction of shark skin (Dean & Bhushan, 2010) and superhydrophobicity of the lotus leaf (Pan, Kota, Mabry, & Tuteja, 2013). In this study, we explore the microscopic surface textures, which can cause drag reduction and superhydrophobicity. We re-create the microscopic surface textures by utilizing interfacial flow instability in drying polyvinylidene fluoride (PVDF) acetone solutions. Typical PVDF films can be made using either spin coating or electrospray deposition with various weight concentrations in acetone.

In order to study the morphology of the porous structure of PVDF films, wet deposition samples were fabricated by spin coating or near-field electrospray. Possible theories were discussed and examined. We proved that the formation of these porous structures is a result of Gibbs-Marangoni convection. Also, we developed a well-controlled method to create porous PVDF films with various pore sizes and pore densities. All samples are characterized and found to exhibit superhydrophobicity and drag reduction. In order to gain a better understanding of porous PVDF film morphology, we connected it to the established field of dry particle fabrication; PVDF particle synthesis by far-field electrospray was also reviewed and discussed. An established method to generate polymer particles of different morphologies by Almería-Díez is confirmed with PVDF as well.

Due to the ability of scalable and re-configurable electrospray, the microscopic surface textures can be applied to areas of any size to reduce drag or impart water-repelling properties.

BIBLIOGRAPHY

- Almería-Díez, B. (2012). *Synthesis of Biodegradable Polymer Micro- and Nanoparticles for Controlled Drug Delivery by Multiplexed Electrosprays*.
- Arun, N., Sharma, A., Pattader, P., Banerjee, I., Dixit, H., & Narayan, K. (2009). Electric-Field-Induced Patterns in Soft Viscoelastic Films: From Long Waves of Viscous Liquids to Short Waves of Elastic Solids. *Physical Review Letters*, 102(25), 254502. doi:10.1103/PhysRevLett.102.254502
- Bassou, N., & Rharbi, Y. (2009). Role of Benard - Marangoni Instabilities during Solvent Evaporation in Polymer Surface Corrugations, (9), 624–632.
- Bormashenko, E., Stein, T., Whyman, G., Bormashenko, Y., & Pogreb, R. (2006). Wetting properties of the multiscaled nanostructured polymer and metallic superhydrophobic surfaces. *Langmuir: the ACS journal of surfaces and colloids*, 22(24), 9982–5. doi:10.1021/la061622m
- Cao, L., Jones, A. K., Sikka, V. K., Wu, J., & Gao, D. (2009). Anti-icing superhydrophobic coatings. *Langmuir: the ACS journal of surfaces and colloids*, 25(21), 12444–8. doi:10.1021/la902882b
- Cha, B, Blades, M., & Douglas, D. J. (2000). An interface with a linear quadrupole ion guide for an electrospray-ion trap mass spectrometer system. *Analytical Chemistry*, 72, 5647–5654.
- Cha, Byungchul, Blades, M., & Douglas, D. J. (2000). An Interface with a Linear Quadrupole Ion Guide for an Electrospray-Ion Trap Mass Spectrometer System 3D ion trap mass spectrometer system is described . The. *System*, 72, 5647–5654. doi:10.1021/ac991409d
- Chauvet, F., Dehaeck, S., & Colinet, P. (2012). Threshold of Bénard-Marangoni instability in drying liquid films. *EPL (Europhysics Letters)*, 99(3), 34001. doi:10.1209/0295-5075/99/34001
- Chen, D. R., Pui, D. Y. H., & Kaufman, S. L. (1995). Electrospraying of Conducting Liquids for Monodisperse Aerosol Generation in the 4 Nm to 1.8 Mu-M Diameter Range. *Journal of Aerosol Science*, 26, 963–977.
- Chirila, D. B. (2010). Introduction to Lattice Boltzmann Methods, 0(1), 1–15.

- Cloupeau, M., & Prunet-Foch, B. (1990). Electrostatic spraying of liquids: Main functioning modes. *Journal of Electrostatics*, 25, 165–184. doi:10.1016/0304-3886(90)90025-Q
- Davies, J. M. (1949). The Aerodynamics of Golf Balls. *Journal of Applied Physics*, 20(9), 821. doi:10.1063/1.1698540
- De La Mora, J. F., & Loscertales, I. G. (1994). The current emitted by highly conducting Taylor cones. *Journal of Fluid Mechanics*, 260, 155–184. doi:10.1017/S0022112094003472
- Dean, B., & Bhushan, B. (2010). Shark-skin surfaces for fluid-drag reduction in turbulent flow: a review. *Philosophical transactions. Series A, Mathematical, physical, and engineering sciences*, 368(1929), 4775–806. doi:10.1098/rsta.2010.0201
- Dean, B. D. (2011). *The Effect of Shark Skin Inspired Riblet Geometries on Drag in Rectangular Duct Flow*.
- Deng, W., & Gomez, A. (2010). The role of electric charge in microdroplets impacting on conducting surfaces. *Physics of Fluids*, 22(5), 051703. doi:10.1063/1.3431739
- Deng, W., Klemic, J. F., Li, X., Reed, M. a., & Gomez, A. (2006). Increase of electrospray throughput using multiplexed microfabricated sources for the scalable generation of monodisperse droplets. *Journal of Aerosol Science*, 37(6), 696–714. doi:10.1016/j.jaerosci.2005.05.011
- Deng, W., Waits, C. M., & Gomez, A. (2010). Digital electrospray for controlled deposition. *The Review of scientific instruments*, 81(3), 035114. doi:10.1063/1.3340907
- Desalination, E., Engineering, B., Engineering, C., & Received, R. O. C. (1995). Pore formation mechanism of membranes from phase inversion process, 103, 233–247.
- Ding, J., Zhang, A., Bai, H., Li, L., Li, J., & Ma, Z. (2013). Breath figure in non-aqueous vapor. *Soft Matter*, 9(2), 506. doi:10.1039/c2sm27093e
- Flows, S. T., & Zhang, N. (2006). Surface tension-driven convection flow in evaporating liquid layers. *Research Signpost*, 661(2), 147–170.
- Gennes, P. G. De. (2001). P HYSICAL J OURNAL E Instabilities during the evaporation of a film : Non-glassy polymer + volatile solvent, 424, 421–424.
- Gomez, A., & Tang, K. (1994). Charge and fission of droplets in electrostatic sprays. *Physics of Fluids*, 6, 404. doi:10.1063/1.868037

- Grampel, R. van de. (2002). Surfaces of fluorinated polymer systems. *Technische Universiteit Eindhoven*. Retrieved from <http://alexandria.tue.nl/extra2/200211249.pdf>
- Gu, X., Raghavan, D., Douglas, J. F., & Karim, a. (2002). Hole-growth instability in the dewetting of evaporating polymer solution films. *Journal of Polymer Science Part B: Polymer Physics*, 40(24), 2825–2832. doi:10.1002/polb.10347
- Higuera, F. J. (2003). Flow rate and electric current emitted by a Taylor cone. *Journal of Fluid Mechanics*, 484, 303–327. doi:10.1017/S0022112003004385
- Hong, Y., Li, Y., Yin, Y., Li, D., & Zou, G. (2008). Electrohydrodynamic atomization of quasi-monodisperse drug-loaded spherical/wrinkled microparticles. *Journal of Aerosol Science*, 39(6), 525–536. doi:10.1016/j.jaerosci.2008.02.004
- Hu, H., & Larson, R. G. (2002). Evaporation of a Sessile Droplet on a Substrate. *The Journal of Physical Chemistry B*, 106, 1334–1344. doi:10.1021/jp0118322
- J.R.A. PEARSON. (1958). On convection cells induced by surface tension.
- Jia, F., & Ben Amar, M. (2013). Theoretical analysis of growth or swelling wrinkles on constrained soft slabs. *Soft Matter*. doi:10.1039/c3sm50640a
- Jiang, L., Zhao, Y., & Zhai, J. (2004). A Lotus-Leaf-like Superhydrophobic Surface: A Porous Microsphere/Nanofiber Composite Film Prepared by Electrohydrodynamics. *Angewandte Chemie*, 116(33), 4438–4441. doi:10.1002/ange.200460333
- Juan, P., & No, X. (1998). Benard–Marangoni convection: planforms and related theoretical predictions, 368, 165–194.
- Ke, B.-B., Wan, L.-S., Zhang, W.-X., & Xu, Z.-K. (2010). Controlled synthesis of linear and comb-like glycopolymers for preparation of honeycomb-patterned films. *Polymer*, 51(10), 2168–2176. doi:10.1016/j.polymer.2010.03.021
- Li, Y., Duan, G., & Cai, W. (2007). Controllable superhydrophobic and lipophobic properties of ordered pore indium oxide array films. *Journal of colloid and interface science*, 314(2), 615–20. doi:10.1016/j.jcis.2007.05.061
- Matar, O. K., Hewitt, G. F., & Ortiz, E. S. (1989). Phase Inversion in Liquid-Liquid Dispersions.
- Mitlin, V. S. (1993). Dewetting of Solid Surface: Analogy with Spinodal Decomposition. *Journal of colloid and interface science*, (156), 491–497.

- Pan, S., Kota, A. K., Mabry, J. M., & Tuteja, A. (2013). Superomniphobic Surfaces for Effective Chemical Shielding. *Journal of the American Chemical Society*, 2, 578–581.
- Pang, C., Lee, G.-Y., Kim, T., Kim, S. M., Kim, H. N., Ahn, S.-H., & Suh, K.-Y. (2012). A flexible and highly sensitive strain-gauge sensor using reversible interlocking of nanofibres. *Nature materials*, 11(9), 795–801. doi:10.1038/nmat3380
- Reiter, G. (1992). Dewetting of Thin Polymer Films. *Physical Review Letters*, 68(1).
- Ristenpart, W., Kim, P., Domingues, C., Wan, J., & Stone, H. (2007). Influence of Substrate Conductivity on Circulation Reversal in Evaporating Drops. *Physical Review Letters*, 99(23), 234502. doi:10.1103/PhysRevLett.99.234502
- Semwogerere, D., & Schatz, M. (2004). Secondary Instabilities of Hexagonal Patterns in a Bénard-Marangoni Convection Experiment. *Physical Review Letters*, 93(12), 124502. doi:10.1103/PhysRevLett.93.124502
- Shan, X. (1997). Simulation of Rayleigh-Benard convection using a lattice Boltzmann method, 55(3), 2780–2788.
- Smolders, C. a., Reuvers, a. J., Boom, R. M., & Wienk, I. M. (1992). Microstructures in phase-inversion membranes. Part 1. Formation of macrovoids. *Journal of Membrane Science*, 73(2-3), 259–275. doi:10.1016/0376-7388(92)80134-6
- Su, B., Sanchez, C., & Yang, X. (2012). *Hierarchically Structured Porous Materials*.
- Sultan, E., Boudaoud, A., & Amar, M. Ben. (2005). Evaporation of a thin film: diffusion of the vapour and Marangoni instabilities. *Journal of Fluid Mechanics*, 543(-1), 183. doi:10.1017/S0022112005006348
- Tang, K., & Gomez, A. (1994). On the structure of an electrostatic spray of monodisperse droplets. *Physics of Fluids*, 6, 2317. doi:10.1063/1.868182
- Taylor, G. (1964). Disintegration of Water Drops in an Electric Field. *Proceedings of the Royal Society A Mathematical Physical and Engineering Sciences*, 280, 383–397. doi:10.1098/rspa.1964.0151
- Temtem, M., Pompeu, D., Jaraquemada, G., Cabrita, E. J., Casimiro, T., & Aguiar-Ricardo, a. (2009). Development of PMMA membranes functionalized with hydroxypropyl-beta-cyclodextrins for controlled drug delivery using a supercritical CO(2)-assisted technology. *International journal of pharmaceutics*, 376(1-2), 110–5. doi:10.1016/j.ijpharm.2009.04.029

THERMOPLASTICS FOR ENGINEERING APPLICATIONS. (n.d.). PERFORMANCE CHARACTERISTICS & DATA.

- Thiele, U. (2003). Open questions and promising new fields in dewetting. *The European physical journal. E, Soft matter*, 12(3), 409–14; discussion 415–6. doi:10.1140/epje/e2004-00009-4
- Thiele, Uwe, Mertig, M., & Pompe, W. (1998). Dewetting of an Evaporating Thin Liquid Film: Heterogeneous Nucleation and Surface Instability. *Physical Review Letters*, 80(13), 2869–2872. doi:10.1103/PhysRevLett.80.2869
- Thomas L. Daniel. (1981). Fish Mucus: In situ Measurements of Polymer Drag Reduction. *Biological Bulletin*, 160(3), 376–382.
- Ting, W.-H., Chen, C.-C., Dai, S. a., Suen, S.-Y., Yang, I.-K., Liu, Y.-L., ... Jeng, R.-J. (2009). Superhydrophobic waxy-dendron-grafted polymer films via nanostructure manipulation. *Journal of Materials Chemistry*, 19(27), 4819. doi:10.1039/b900468h
- Tuteja, A., Choi, W., Ma, M., Mabry, J. M., Mazzella, S. a, Rutledge, G. C., ... Cohen, R. E. (2007). Designing superoleophobic surfaces. *Science (New York, N. Y.)*, 318(5856), 1618–22. doi:10.1126/science.1148326
- Vrij, a., & Overbeek, J. T. G. (1968). Rupture of thin liquid films due to spontaneous fluctuations in thickness. *Journal of the American Chemical Society*, 90(12), 3074–3078. doi:10.1021/ja01014a015
- Whyman, G., & Bormashenko, E. (2011). How to make the Cassie wetting state stable? *Langmuir: the ACS journal of surfaces and colloids*, 27(13), 8171–6. doi:10.1021/la2011869
- Wong, K. H., Davis, T. P., Barner-Kowollik, C., & Stenzel, M. H. (2007). Honeycomb structured porous films from amphiphilic block copolymers prepared via RAFT polymerization. *Polymer*, 48(17), 4950–4965. doi:10.1016/j.polymer.2007.06.048
- Xu, L., Shi, T., Dutta, P. K., & An, L. (2007). Rim instability by solvent-induced dewetting. *The Journal of chemical physics*, 127(14), 144704. doi:10.1063/1.2770734
- Xue, Z., Liu, M., & Jiang, L. (2012). Recent developments in polymeric superoleophobic surfaces. *Journal of Polymer Science Part B: Polymer Physics*, 50(17), 1209–1224. doi:10.1002/polb.23115
- Zeleny, J. (1917). Instability of Electrified Liquid Surfaces. *The Physical Review*, X(10), 1–6.

Zhang, S., You, B., Gu, G., & Wu, L. (2009). A simple approach to fabricate morphological gradient on polymer surfaces. *Polymer*, 50(26), 6235–6244. doi:10.1016/j.polymer.2009.11.003